Exploration of driving mechanisms of equilibrium boron isotope fractionation in tourmaline group minerals and fluid: A density functional theory study

Yin-Chuan Li [a], Hong-Wei Chen [b], Hai-Zhen Wei [a] *, Shao-Yong Jiang [c] *, Martin R. Palmer [d],

T. G. M. van de Ven [e], Simon Hohl [a], Jian-Jun Lu [a], Jing Ma [b] *

[a] *State Key Laboratory for Mineral Deposits Research, Department of Earth Sciences and Engineering, Nanjing University, Nanjing 210023, PR China*

[b] *Key Laboratory of Mesoscopic Chemistry of MOE, School of Chemistry & Chemical Engineering, Nanjing University, Nanjing, 210023, PR China*

[c] *State Key Laboratory of Geological Processes and Mineral Resources, Faculty of Earth Resources, China University of Geosciences, Wuhan 430074, PR China*

[d] *School of Ocean and Earth Science, NOC, University of Southampton, European Way, Southampton SO14 3ZH, UK*

[e] *Department of Chemistry, McGill University, Montreal, Quebec H3A 2A7, Canada*

* Author to whom correspondence should be addressed:
Profs. Hai-Zhen Wei, Jing Ma
School of Earth Sciences and Engineering, School of Chemistry & Chemical Engineering, Nanjing University
163 Xianlin Avenue, Nanjing, Jiangsu, 210023 PR China
Phone: +86 (25) 89681617; Fax: +86 (25) 89682393
Email address: haizhenwei@nju.edu.cn; majing@nju.edu.cn
Prof. Shao-Yong Jiang
State Key Laboratory of Geological Processes and Mineral Resources,

Faculty of Earth Resources, China University of Geosciences, Wuhan 430074, PR China
Email address: shyjiang@cug.edu.cn

ABSTRACT

The equilibrium boron isotope fractionations ($\alpha_{3-4,}$ $\Delta^{11}B_{(tour\text{-}fluid)}$) between tourmaline mineral groups and fluids at 0.5 GPa, 600-1000 K are investigated using density functional theory calculations. The first solvent shell controls boron isotope fractionation in solution, with the β values of both H_3BO_3 and $B(OH)_4^-$ decrease with increasing numbers of hydrogen bonds. In supercritical fluids, the weakening of hydrogen bonds and the diversity in configurations of hydrated boron species both contribute to variations in the vibrational frequencies. The $1000\ln\alpha_{Tur\text{-}fluid}$ value increases with increasing Mg/(Fe+Mg) ratios in the dravite-schorl solid solution series. This effect, together with the crystallization sequence predicted from the Gibbs free energies of tourmaline formation, accounts well for the association of boron isotope and chemical zonation observed in zoned tourmaline grains. The dependence of boron isotope fractionation on the B-O bond length in tourmaline group minerals reflects the changes in relevant molar volumes caused by differences in the mass and charge of the atoms occupying the *X*, *Y*, and *Z* sites of tourmalines. This study suggests that the chemical composition of the tourmaline plays an important role in controlling the boron isotope composition in tourmalines crystallized from hydrothermal systems.

Keywords: Boron isotope fractionation; Reduced partition function ratio (RPFR); Tourmaline group minerals; Fluid

INTRODUCTION

Boron has two stable isotopes, ^{10}B and ^{11}B, whose abundances are approximately 20% and 80%, respectively. Because of the large relative mass difference between ^{10}B and ^{11}B, significant fractionation between boron-bearing solid minerals and fluids occurs in nature (Palmer and Swihart, 2002; Marschall and Jiang, 2011). Tourmaline is the most important boron-bearing mineral in the crust and commonly occurs in various rock types and mineral deposits. The wide stability range, resistance to alteration and variable composition of tourmaline make it a useful tool to investigate records of igneous, metamorphic and metallogenic processes (Henry and Guidotti, 1985; Slack 1996; Marschall and Jiang, 2011). The general tourmaline formula can be expressed as, $XY_3Al_6(BO_3)_3Si_6O_{18}(OH,F)_4$, and the most abundant tourmaline solid solutions can be written as $Na(Mg,Fe)_3Al_6(BO_3)_3Si_6O_{18}(OH,F)_4$.

Because of the sensitivity of boron isotopes to changes in the fluid source, P-T conditions of crystallization, and phase transitions, boron isotope studies of tourmalines have been used to track the origins of late magmatic and magmatic-hydrothermal fluids which play a critical role in ore-forming processes (e.g., Palmer and Slack, 1989; Palmer and Swihart 2002; Slack 1996; Smith and Yardley, 1996; Jiang et al., 2000; Lambert-Smith, 2016; Su et al., 2016; Zheng et al., 2016; Molnár et al., 2016). In addition, the boron isotopic composition of tourmaline can unravel complex petrologic histories of deeply subducted lithologies (Bebout and Nakamura, 2003). As well as the composition of the source rocks, other factors that influence boron isotope compositions of tourmaline include the water/rock ratio (i.e., the volume ratio of fluid to rocks), temperature, pressure, multiple-stages of tourmaline formation, dynamic isotope fractionation (e.g., Rayleigh fractionation), seawater entrainment, alteration and metamorphism, and phase separation of hydrothermal fluids (Jiang, 2001). The effects of temperature, pressure, Rayleigh fractionation, and liquid-vapor fractionation have been investigated experimentally (Palmer et al., 1992; Bebout and Nakamura, 2003; Liebscher et al., 2005; Meyer et al., 2008; Krienitz et al., 2008; Kowalski and Wunder, 2018) and the results indicate that they all play a role in defining the boron isotope compositions of tourmalines.

Another important observation in hydrothermal deposits is that the boron isotope zonation of tourmaline commonly exhibits a close association with chemical zonation (Smith and Yardley, 1996; Xavier et al., 2008; Mercadier et al., 2012; Yan and Chen, 2014; Zheng et al., 2016; Su et al., 2016). One of the most common manifestations of this zonation is the presence of Fe-rich cores and Mg-rich rims, with the rim of the zoned tourmaline often showing notably lower $\delta^{11}B$ values than the core (e.g., Yan and Chen, 2014; Nakano and Nakamura 2001). It is important to note, however, that negligible isotopic variation in chemically zoned tourmaline has also been reported (e.g., Tonarini et al., 1998). In addition to Fe and Mg, other metals (e.g., Na, Ca, and Al) also show relationships with the boron isotope composition of tourmaline (e.g., Molnár et al., 2016). The complex site substitutions of tourmaline, which can be expressed with exchange vectors (Henry and Dutrow, 2012) such as $FeMg_{-1}$, $AlFe_{-1}$, $\square Al(NaFe)_{-1}$ etc., however, make interpretation of the relationship between the chemical composition and boron isotope composition of tourmaline complex. However, while it is possible to control temperature and pressure during tourmaline synthesis (Palmer et al., 1992; Schreyer et al., 2000; Meyer et al., 2008), it is difficult to control the chemical composition of tourmalines during hydrothermal experiments, and different synthesis techniques can result in both equilibrium and non-equilibrium isotope and chemical fractionations (Meyer et al., 2008).

Quantum mechanics calculations offer an alternative approach to explore the isotope fractionation mechanisms on the atomic scale, such as H isotope fractionation between hydrous minerals and vapor (Méheut et al., 2010), Si and O isotope fractionations in silicates (Méheut et al., 2007, 2009, 2014), Fe isotope fractionations in common Fe-bearing minerals (Blanchard et al., 2009, 2012), stable Si and Mg isotopes fractionation in mafic minerals and phase transformation (Huang et al., 2013, 2014; Wu et al., 2015), equilibrium Ge and Se isotopes fractionation (Li et al., 2009, 2011) and isotopic fractionation in adsorption and thermal diffusion processes (Li et al., 2010, 2011, 2015) etc. This approach has also been applied to boron isotope fractionation between various minerals and mineral-fluids systems, and has contributed towards understanding geochemical mechanisms (see Kowalski and Wunder (2018) for a recent summary).

In theoretical calculations, the models used to represent minerals and fluids are pivotal, because the minerals have discrete compositions, whereas fluids have a continuum of compositions, leading to an infinite array of potential model conditions. In minerals systems, the periodic boundary conditions (PBC) method has generally been used in a lattice dynamics context to produce accurate theoretical isotope fractionations between minerals. Because the bond length and angle variations in silicates are governed mainly by the local atomic arrangement in crystalline lattices (Gibbs, 1982), a new method of representing the mineral environment with molecular clusters (based on conservation of Pauling bond strength) was introduced to crystalline system by Rustad et al. (2008). This method has been refined within the local atomic structure of minerals and/or fluids to carry out electronic structure calculations of the equilibrium isotope fractionations between different minerals and aqueous solutions (Rustad et al., 2010a). The molecular cluster models increase the flexibility of using molecular codes for calculation models of solid-state systems and allows relatively seamless integration of calculation among different phases. This approach has been applied to predict isotope fractionations in surficial geological processes under lower T and P conditions (e.g., Fe isotope fractionation between hematite and ferric and ferrous in aqueous solution (Rustad and Dixon, 2009), C isotope fractionation in CO_2, aqueous carbon species and carbonate minerals (Rustad et al., 2008), Mg isotope fractionations between minerals and aqueous solutions by Gao et al., 2018, and Mg, Ca and Fe isotope fractionation among carbonate minerals (Rustad et al., 2010a)). In addition, this method has been shown to be applicable to understanding Fe isotope fractionation in the Earth's lower mantle at temperatures of up to 4000 K and pressures as high as 120 GPa (e.g., Rustad and Yin, 2009).

In aqueous fluids, the isolated cluster approach is used, in which the selected species is surrounded by a hydration shell and the whole structure is optimized at 0 K (Kowalski and Jahn, 2011 and references therein). After predicting fractionation factors in aqueous solution based on the computation of static configurations using theoretical methods such as density functional theory (DFT) or Hartree-Fock molecular orbital (HF-MO) theory, Møller-Plesset (MP2) (Liu and Tossell, 2005; Zeebe, 2005; Klochko et al., 2006; Rustad and Bylaska, 2007; Zeebe, 2009, 2010 etc.), the impact of dynamic behaviors of particles and compressibility of fluids has been recognized widely, especially at high temperature and pressure conditions (Jahn and Wunder, 2009; Wunder et al., 2011). The *ab initio* molecular dynamics (AIMD) method is considered to be a powerful tool with which to explore the hydration effect and speciation/complexation in hydrothermal fluids (e.g., Mei et al., 2013, 2015, 2016, 2017, 2018). The pioneering work by Rustad and Bylaska (2007) accounted for the dynamic effects on isotope fractionation in fluids by computing the harmonic frequencies of selected configurations along the molecular dynamic trajectory of AIMD at ambient conditions. The AIMD simulation approach has subsequently been used to predict equilibrium Li and B isotope between minerals and fluids at high P and T condition (e.g., Kowalski and Jahn, 2011; Kowalski et al., 2013).

In addition to theoretical calculations of simple crystals containing only a few atoms in the unit cell, the pioneering work by Kowalski et al. (2013) was the first to predict the equilibrium boron isotope fractionation between complex crystalline boron-bearing minerals (e.g., tourmaline and mica) and fluids with PBC models (Kowalski et al. 2013). The study of Kowalski et al. (2013) indicated that the isotope fractionation is mainly driven by the coordination of the boron atoms, the degree of isotope fractionation is strongly correlated with the B-O bond length, and that the PBC computational scheme is also capable of predicting the isotopic signatures at extreme conditions and gives valuable insights into the processes governing the isotope fractionation mechanisms on the atomic scale. Because of the complex site substitutions within tourmaline, and the close association between boron isotope and chemical zonation observed in tourmaline, the temperature-dependent equilibrium boron isotope fractionation between tourmaline group minerals and fluid was re-investigated with cluster models in this work, emphasizing the hydration effect on the RPFRs and $\alpha_{3\text{-}4}$ factors, and the changes in vibrational frequency modes induced by the weakening of hydrogen bonds in supercritical fluids. The influence of chemical composition on equilibrium fractionation of boron isotopes, the underlying mechanisms driving the equilibrium processes, as well as its wider implication for hydrothermal mineral-deposits are explored here.

2. COMPUTATIONAL METHODS

2.1 Calculation of the reduced partition function ratio (RPFR)

Applying the theory of Bigeleisen and Mayer (1947), the equilibrium isotope fractionation factor for an isotope exchange reaction can be calculated. For example, there is a boron isotope exchange reaction, and if there is only one boron atom in the structure of X (such as $B(OH)_3$) and three boron atoms in the structure of Y (such as $NaMg_3Al_6(BO_3)_3Si_6O_{18}(OH)_4$):

$$nX + Y^* \Leftrightarrow nX^* + Y \qquad \text{(Eq. 1)}$$

where X and Y are molecules or minerals, X and Y indicate the substances containing the lighter isotope (^{10}B) and X^* and Y^* indicate the substances containing the heavier isotope (^{11}B), n is the number of boron atoms (^{11}B) substituted in Y^*.

The isotope fractionation factor (α) for the general isotope exchange reaction between X and Y can then be written as (Liu and Tossell, 2005):

$$\alpha = \frac{RPFR(X)}{RPFR^{\frac{1}{n}}(Y)} = \beta(X)/\beta(Y) \qquad \text{(Eq. 2)}$$

where the reduced isotopic partition function ratio ($RPFR$, or β factor) of X and Y are given by:

$$RPFR(X) = \frac{Z^*}{Z} = \prod_i^N \frac{\mathrm{u}_i^*}{\mathrm{u}_i} \frac{\exp(-\frac{\mathrm{u}_i^*}{2})}{1-\exp(-\mathrm{u}_i^*)} \frac{1-\exp(-\mathrm{u}_i)}{\exp(-\frac{\mathrm{u}_i}{2})} \qquad \text{(Eq. 3)}$$

where Z (Z^*) is the partition function of X (X^*), N is the total number of vibration modes in X, and subscript i is the vibration mode order number. For convenience of expression, the $RPFR$ or $RPFR^{1/n}$ is replaced by β factor. The term of u_i (u^*_i) can be calculated by:

$$u_i = \frac{hc \cdot \upsilon_i}{kT} \qquad \text{(Eq. 4)}$$

where h is Plank's constant, c is the speed of light, υ_i is the frequency of vibration, subscript i is the number of vibration mode, k is Boltzmann's constant and T is environment temperature in degrees Kelvin.

The isotopic composition of boron is expressed as per mil deviations from the boric acid standard reference material NIST SRM 951:

$$\delta^{11}B(‰) = \left(\left(\frac{{}^{11}\mathrm{B}/{}^{10}\mathrm{B}_{\mathrm{sample}}}{{}^{11}\mathrm{B}/{}^{10}\mathrm{B}_{\mathrm{standard}}} \right) - 1 \right) \times 10^3 \qquad \text{(Eq. 5)}$$

Given the variation of δ^{11}B from -60 ‰ to +60 ‰ in nature, the approximation of ln(δ^{11}B+1) ≅ δ^{11}B is valid. The relation of the boron isotope fractionation factor ($\alpha_{\text{Tur-fluid}}$) between tourmaline and fluid and the extent of boron isotope fractionation between the two phases ($\Delta_{Tur-fluid}$) can be expressed by Eq. 6:

$$1000\ln\alpha_{Tur-fluid} \cong \delta^{11}B_{Tur} - \delta^{11}B_{fluid} = \Delta_{Tur-fluid} \qquad \text{(Eq. 6)}$$

2.2. Representation of the mineral and aqueous environments

2.2.1. Representation of aqueous fluid at ambient and supercritical conditions

Cluster models of $B(OH)_3 \cdot nH_2O$ and $B(OH)_4^- \cdot nH_2O$ (n=30~33) with different numbers of hydrogen bonds were constructed to represent the aqueous fluid at ambient conditions. In order to generate the configurations of a supercritical fluid (i.e. 0.5 GPa, 600-1000 K), *ab initio* molecular dynamics (AIMD) simulations were carried out. The aqueous solution was represented by a periodically repeated box that containing one H_3BO_3 or one $B(OH)_4^-$ molecule surrounded by 40 water molecules (Figure A1), which is sufficient to consider the short-range effect of water solvents (Rustad et al., 2007, 2010b; Kowalski et al., 2013). In order to achieve realistic conditions in the supercritical fluids with a slight change in the box volumes, the AIMD simulation in the NVT ensemble started from a temperature of 300 K and increased gradually with a temperature increment interval of 100 K by implementing sequential AIMD runs with NPT simulations of 0.06 ps (Figure A2). The 10 ps of AIMD simulation trajectories were then computed in the NVT ensemble to acquire representative configurations of the supercritical fluids at 600 K, 800 K and 1000 K, respectively. To ensure the convergence of the MD simulation of the conformational distribution, the variations of intramolecular B---O bond length of aqueous H_3BO_3 and $B(OH)_4^-$ in 10 ps MD simulation trajectory were compared (e.g., at 0.5 GPa and 600 K in Figure A3). Finally, ten representative configurations of fluid were extracted from each of the AIMD trajectories and were shown to be uncorrelated (Figure A4). The periodic boundary conditions were removed, and only the solute (H_3BO_3 or $B(OH)_4^-$) and the surrounding H_2O molecules were maintained, especially for those closest to the first solvent shell. The water molecules of all cluster models were fixed at a high T-P position to represent a supercritical environment.

2.2.2. Representation of tourmaline

Both the primitive cell with the periodic boundary condition (PBC) and the cluster model of dravite were built for comparison. During the construction of a representative cluster to represent the tourmaline crystalline structure, some primitive bonds within the larger crystal lattice are broken and produce isolated fractional charges. A total of 57 hydrogen atoms were added onto the positions of breaking bonds in order to neutralize these charges and obtain a neutral and self-compensated cluster. The mineral model was optimized without any deformation of cationic ion coordination polyhedra and the effect of additional hydrogen atoms on the basic structure has been verified to be negligible on the results presented below. Larger mineral cluster models that consist of a primitive cell without fixing any atoms is an alternative approach for isotope fractionation calculation, as discussed below.

The general chemical formula of tourmaline can be abbreviated as $XY_3Z_6[T_6O_{18}][BO_3]_3V_3W$ (Rajajee et al., 1999), where X, Y, Z, T, B, V and W represent the sites within the asymmetric unit of the structure, and have variable atoms in each of sites in different varieties of tourmaline (e.g., schorl, dravite, etc.). It has been shown that the local vibration modes can be affected by atoms that are at most two or three bonds away, because different isotopically substituted molecules only differ in the IR vibrational energies (Liu and Tossell, 2005). In order to investigate the equilibrium boron isotope fractionation between tourmalines and fluids, the nearest neighbor atoms of three boron atoms are included in our tourmaline model, which can be divided into three layers:

$$XY_3Z_6[T_6O_{18}][BO_3]_3V_3W+X_0Y_0Z_6[T_0O_{24}][B_0O_4]_3V_3W_0+57H$$

In which, the central structure is $XY_3Z_6[T_6O_{18}][BO_3]_3V_3W$ based on the chemical formula of tourmaline. $X_0Y_0Z_6[T_0O_{24}][B_0O_4]_3V_3W_0$ can then be used to express the influences from the adjacent three tourmaline molecules. The additional 57 hydrogen atoms are added to keep charge neutrality and avoid any structural deformation. For dravite, X = Na Y = Mg Z = Al T = Si B = B V = OH W = OH, and the molecular cluster model is shown in Figure A5. Here, we only consider the situation of Z = Al T = Si, because these are by far the most common forms of tourmaline in nature. For tourmaline group minerals, the model for schorl is constructed by replacing the three Mg atoms of the dravite model by three Fe atoms, and these of dravite+Fe and schorl+Mg models are constructed by replacing one Mg atom of the dravite model with one Fe atom and by replacing one Fe atom of the schorl model with one Mg atom, respectively. The model of hydroxy-liddicoatite is constructed by the substitution of $(CaLi_2)(NaMg_2)_{-1}$ into the dravite model while that of olenite is constructed by the substitution of $(Al)_3(Mg^{V}H)_{-3}$ into the dravite model, in which ^{V}H represents a hydrogen atom of OH^- in the V sites.

2.3. DFT calculation of electronic structures

For minerals, the PBC model of dravite was built using Materials Studio (Accelrys, Inc., version 7.0) with known lattice parameters (Bosi et al., 2005), which has a cell size of 9.52742 Å in each dimension and equal angles of 113.95658°. The Brillouin zone (BZ) was sampled with a 2 × 2 × 2 k-point for geometry optimization and the energy cut-off for the plane wave basis set was 800 eV. The generalized gradient approximation (GGA) method together with the Perdew-Burke-Ernzerhof (PBE) exchange-correlation function, and the norm-conserving pseudopotentials were employed in both geometry optimizations and phonons calculation of the PBC model of dravite. The calculation of PBC model of dravite was carried out using the Cambridge Serial Total Energy Package (CASTEP). In addition, the geometry optimizations and vibrational frequencies and the Gibbs free energies calculation of the cluster models of tourmaline group minerals were calculated by the B3LYP exchange-correlation functional with 6-31G(d) basis set in GAUSSIAN 16 software package (Frisch et al., 2016). After computing frequencies following a previous geometry optimization with the same functional/basis set using Gaussian 16 software package, the relevant vibrational spectra with the default peak-width at half height is 15 cm^{-1} (such as IR, Raman, VCD etc.) could be exported through Gaussian View. At the specified temperature (298.15 K by default), thermochemistry analysis follows the frequency and normal mode data. The Gibbs free energy can then be calculated on the basis of thermal-corrected energy and entropy computed with the Gaussian program. The statistical mechanics for thermochemistry analysis has been demonstrated by McQuarrie and Donald (1973).

For fluids, the static cluster models of aqueous fluid were calculated with the level of B3LYP/6-31G(d) at ambient conditions. In the supercritical fluid, the AIMD trajectories of $H_3BO_3\cdot$ 40 H_2O and $B(OH)_4^-\cdot$40 H_2O were calculated with the level of PBE/norm-conserving pseudopotentials (the same functional and pseudopotentials with the PBC model of dravite) at 0.5 GPa and 600 K, 800 K and 1000 K. Because the PBE functional does not describe weak interactions (e.g., van der Waals interaction) very well, the DFT-D method within the 'Grimme scheme' was applied to provide the best compromise between the cost of first principles evaluation of the dispersion terms and the need to improve non-bonding interactions in the standard DFT description (Grimme, 2006). At each thermodynamic condition, at least 10 ps long trajectories were generated with an integration step of 0.12 fs and ten individual configurations of supercritical aqueous fluid were respectively extracted from each of the AIMD trajectories. The PBC of representative configurations were removed and only a solute (H_3BO_3 or $B(OH)_4^-$) and 40 H_2O molecules, especially for those close to the first solvent shell, were maintained. The solute species ((H_3BO_3 or $B(OH)_4^-$) was relaxed while the water molecules of all cluster models were still fixed at the primitive high P-T positions, so as to better represent a supercritical environment. On the basis of the comparison on calculated RPFR and $\alpha_{3\text{-}4}$ of aqueous H_3BO_3 and $B(OH)_4^-$ using different levels of functional/basis set (as discussed in S3 and Table A1 in the Appendix), the vibrational frequencies and the IR spectra were calculated by the B3LYP exchange-correlation functional with 6-31G(d) basis set using the GAUSSIAN 16 software package (Frisch et al., 2016).

For comparison, the GGA function (PBE, BLYP) and the hybrid function (B3LYP), with different basis sets, were used for computation of vibrational frequencies of isolated and aqueous $B(OH)_3$ and $B(OH)_4^-$ species.

2.4. Error estimations

The errors in the calculated values of the RPFRs (i.e., β factor) and boron isotope fractionation factors (i.e. $\alpha_{3\text{-}4}$, $\Delta^{11}B_{(\text{tour-fluid})}$) were estimated from the average deviation of repeated calculations. The absolute standard errors in $\alpha_{3\text{-}4}$ factors of isolated and aqueous H_3BO_3 and $B(OH)_4^-$ at ambient conditions were ca. ± 0.0066 ‰ (2σ from replicate calculations with the same level of functional/basis set (e.g., B3LYP, BLYP, PBE, X3LYP, BP86, PW91 etc., Table A2), in a good agreement with the estimated absolute error of ± 0.008 ‰ in $\alpha_{3\text{-}4}$ factor by Kowalski et al. (2013) (i.e. $\alpha_{3\text{-}4} = 1.032 \pm 0.008$). In supercritical fluid, the errors in β and $\alpha_{3\text{-}4}$ factors of H_3BO_3 and $B(OH)_4^-$ were estimated from the vibrational frequencies calculated for the individual configurations generated by the AIMD. The relative errors of $\alpha_{3\text{-}4}$ are ± 0.035%, ± 0.025% and ± 0.012% at 600, 800 and 1000 K, respectively. As evaluated, the relative errors of (α-1) are 29% and 33% of the (β-1) factors at 600 K and 1000 K, respectively; showing good agreement with the estimates of computational errors (25% and 36%) by Kowalski et al. (2013). For the minerals, the absolute errors in β were less than 1.5 ‰ as estimated from cluster models with B3LYP functional and from PBC with PBE/Troullier-Martins pseudopotentials.

The overall errors in $\Delta^{11}B_{(tour\text{-}fluid)}$ estimated by the error propagation are ± 1.9‰, ± 1.7‰ and ± 1.0‰ at 600 K, 800 K and 1000 K, respectively, and are similar to the error estimates suggested by Kowalski et al. (2013).

3. RESULTS

3.1. Calculation of RPFRs of fluid models at ambient and supercritical conditions

Because changes in the number of hydrogen bonds between $B(OH)_3$ and H_2O and $B(OH)_4^-$ and H_2O may affect the reduced partition function ratios (RPFR) in fluids, a series of static models with one $B(OH)_3$ or $B(OH)_4^-$ and variable water molecules (nH_2O, n is an integer) were built to simulate the variability of the number of hydrogen bonds around boron species at 300 K. In order to clarify the solvent effect on boron isotope fractionation, the RFPRs of hydrated H_3BO_3 and $B(OH)_4^-$ with different water molecules (p) and hydrogen bonds (q) calculated with B3LYP/6-31G(d) are compared in Table A3. There is no clear difference in the RFPRs of hydrated H_3BO_3 (i.e. β3) and $B(OH)_4^-$ (i.e. β4) with variation of the number of H_2O within the statistical error of ± 0.7 ‰, and both β3 and β4 values decrease with an increase in the number of hydrogen bonds. As a result, the $\alpha_{3\text{-}4}$ of aqueous H_3BO_3 and $B(OH)_4^-$ varied from 1.0239 to 1.0277, and will be discussed further below.

According to the AIMD trajectories, the RPFRs were computed on ten of the ionic cluster configurations extracted along the AIMD trajectories, and the average RPFRs of hydrated H_3BO_3 and $B(OH)_4^-$ at temperatures of 600 K, 800 K and 1000 K can be found in Table A4 and Figure A6a. The resulting boron isotope fractionation factors $\alpha_{3\text{-}4}$ are parallel to those obtained in previous studies as shown in Figure A6b. After correcting the dataset of Sanchez-Valle et al. (2005) by the relationship of $\Delta\alpha = 16.4\times2(300/T)^2$ (as proposed by Kowalski et al. (2013)), the $1000\ln\alpha_{3\text{-}4}$ values at 1000 K are consistent with previous studies (Kowalski et al., 2013;

Sanchez-Valle et al., 2005), with a discrepancy of < 1.25 ‰ over the temperature range considered.

3.2. Calculation of RPFRs of tourmaline group minerals models

The difference in β factors obtained from PBC supercell and cluster models are ~±0.5 ‰ at 1000 K and ~±1.0 ‰ at 600 K (Figure A7), equivalent to negligible differences of ~±0.1 ‰ at 1000 K and ±0.2 ‰ at 600 K in the α values, following the estimation of computational error by Kowalski et al. (2013). In order to differentiate the three boron atoms in tourmaline, and to better understand the influence of adjacent metal atoms on boron isotope fractionation, we used a representing method for the boron atom, as illustrated in Figure A8. This shows one local structure of the dravite+Fe model whose upper structure is concealed so the boron atoms are easily displayed. The one boron atom labelled as 88 (or 89, 90) was marked as Mg-Mg-88(or Mg-Fe-89, Mg-Fe-90) and the two boron atoms labelled as 88 and 89 (88 and 90, 89 and 90) are marked as Mg-Mg-Fe-88+89 (Mg-Mg-Fe-88+90, Mg-Fe-Mg-89+90). When all three boron atoms labelled as 88, 89 and 90 were replaced, 88+89+90 was used. The calculated RPFRs and boron isotope fractionation factors ($1000\ln\alpha_{\text{Tur-fluid}}$) between dravite (schorl) and fluids by replacing one ^{11}B in dravite (schorl) model are then listed in Table A5-A8.

In order to better quantify any shifts induced by the change of metal atoms around one boron atom, the boron isotope fractionation factors of different tourmaline models were calculated by replacing one ^{11}B atom and 2 or 3 ^{11}B atoms in the tourmaline models. The results indicate that the boron isotope fractionation between the different *B* sites is negligible (Tables A5, A6, A7). Therefore, a model including only one boron atom and its next nearest neighbor (NNN) atoms is sufficient to represent one local repeated unit of a tourmaline structure.

4. DISCUSSION

4.1. Dominant factors that influence on RPFRs and $\alpha_{3\text{-}4}$ *in the aqueous fluid*

In a mineral-fluid system, the level of computational treatment of the aqueous environment is more important than treatment of the mineral environment in determining the overall quality of the predicted mineral–aqueous isotope fractionation (Rustad et al., 2010a). In solution, the $\alpha_{3\text{-}4}$ of aqueous H_3BO_3 and $B(OH)_4^-$ obtained from experimental and theoretical approaches varies in a wide range from 1.0255 to 1.0324 (Table A1), and this discrepancy raises concerns regarding the solution matrices and the calculation setup. Early studies showed that the $\alpha_{3\text{-}4}$ for seawater matrices is slightly larger than that of pure water (ranging from ~1.0255 to ~1.027) and different cations have slightly different, but minor effects on $\alpha_{3\text{-}4}$ (Liu and Tossell, 2005). Later experiments suggested that the relatively weak ion pairing of borate with major seawater cations has a negligible influence on the fractionation factor, and an $\alpha_{3\text{-}4}$ value of 1.0272 ± 0.0006 was determined for synthetic seawater at 25°C (Klochko et al., 2006). This value is in good agreement with both the theoretical mean of 1.0279 ± 0.0028, and the experimental mean of 1.0271 ± 0.0010 (see Table A1), and has been widely accepted. Note that polymeric boron species in solutions formed when boron concentrations exceed 0.025 M, are not likely to occur in natural systems other than in evaporitic deposits (Felmy and Weare, 1986). Recent studies imply that the first hydration shell (e.g., coordination configuration, coordination bond and coordination number) may affect the physicochemical properties of hydrated ions (or molecules), including the basic vibration modes involved in the isotope fractionation calculations (e.g., Pye and Rudolph, 2001; Kubicki, 2001; Zhou et al., 2006; Vchirawongkwin and Rode, 2007; Miller et al., 2007; Rustad and Bylaska, 2007; Rustad et al., 2008, Pinilla et al., 2015; Kowalski and Jahn 2011; Dupuis et al., 2015). This will be discussed further below.

4.1.1. Influence of the first solvent shell on RPFRs and $\alpha_{3\text{-}4}$ *in fluid at ambient condition*

To better evaluate the calculation quality, the computed and measured vibrational frequencies for both isolated and aqueous H_3BO_3 and $B(OH)_4^-$ species are compared in Figure 1 and Table

A9 in the range of 400 to ~1000 cm $^{-1}$. The larger discrepancies at higher frequencies for the antisymmetric B-O stretch mode at ~1470 cm^{-1} agree well with a previous study (Rustad et al., 2010b), and is thought to reflect the harmonic DFT frequencies versus the anharmonic experimental frequencies, and/or the strong basis set dependence of calculated frequencies (Rustad et al., 2010b).

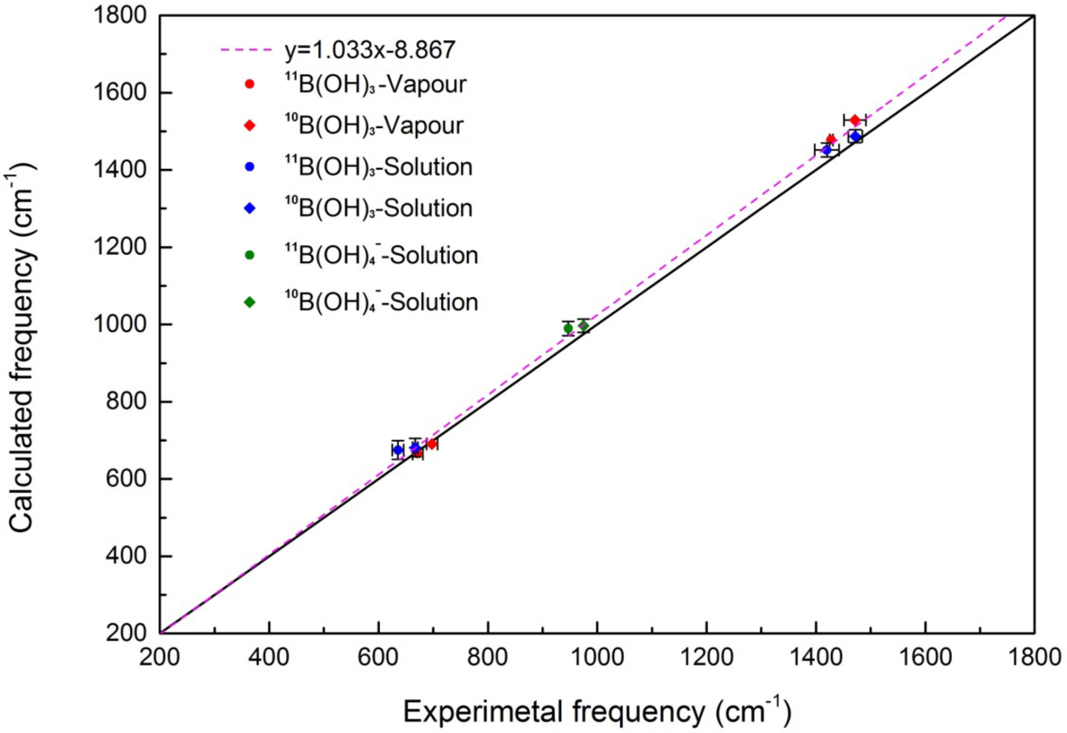

Figure 1. Comparison on measured and computed vibrational frequencies for both isolated and aqueous H_3BO_3 and $B(OH)_4^-$ species at ambient condition. Experimental data are cited from previous contributions (Kowalski et al., 2013 and references within). Theoretical values were calculated from clusters by B3LYP/6-31G(d).

At high T and P conditions, the coordination number of water increases with increasing temperature and pressure, as verified by studies of Li isotope fractionation (Kowalski et al., 2011; Jahn and Wunder, 2009). Both the β3 and β4 values decrease with an increase in the number of hydrogen bonds at ambient condition, as shown in Figure A9. The calculated the

RPFRs of both H_3BO_3 and $B(OH)_4^-$ decrease by 1.97% and 1.43% due to the hydration effect, which is consistent with values of 1.5% and 1.2% determined by Oi and Yanase (2001). When comparing the IR spectra of isolated H_3BO_3 and aqueous H_3BO_3 with different numbers of hydrogen bonds at the ambient condition (Figure A10), the vibrational frequencies of symmetric bending (δ-B at ~503 cm^{-1}), out-of–plane bending (γ-BO at ~632 cm^{-1}), and asymmetric stretching (ν_a-BO at ~1412 cm^{-1}) of aqueous H_3BO_3 show a blue-shift compared to the isolated H_3BO_3 molecule. With increasing numbers of hydrogen bonds, frequencies from the OH-B-OH antisymmetric stretching mode (at ~1524 cm^{-1}) and the OH stretching vibrational mode (at ~3200 cm^{-1}) appear, contributing to the RPFRs of aqueous H_3BO_3. For a constant number of hydrogen bonds in aqueous H_3BO_3 (i.e., q_{BIII} is a constant), $\alpha_{3\text{-}4}$ increases with an increasing number of hydrogen bonds in aqueous $B(OH)_4^-$ with an average slope of $\frac{d\alpha_{3-4}}{dq_{BIV}} = 0.082 \times 10^{-3}$, while for a constant number of hydrogen bond in aqueous $B(OH)_4^-$ (i.e., q_{BIV} is a constant), $\alpha_{3\text{-}4}$ decreases with an increasing number of hydrogen bonds in aqueous H_3BO_3 with an average slope of $\frac{d\alpha_{3-4}}{dq_{BIII}} = -0.56 \times 10^{-3}$. This illustrates that the hydration effect of aqueous H_3BO_3 is an order of magnitude greater than that from $B(OH)_4^-$. With the variable q numbers in H_3BO_3 and $B(OH)_4^-$, the $\alpha_{3\text{-}4}$ varies from 1.0239 to 1.0277 (Table A3), and the maximum difference of 3.7 ‰ in $\alpha_{3\text{-}4}$ induced from the hydration effect argues against negligible hydration effects on boron isotope fractionation (~0.5 ‰) (Oi and Yanase, 2001).

4.1.2. Influence of configuration of hydrated boron species on the RPFRs and $\alpha_{3\text{-}4}$ in supercritical fluid

Unlike isolated and aqueous boron species at ambient conditions, the radial distribution functions of aqueous H_3BO_3 and $B(OH)_4^-$ from the AIMD simulations of the supercritical fluids (i.e. 0.5 GPa-600K, 0.5 GPa-800K, 0.5 GPa-1000K) show that the first solvent shell becomes less well defined with increasing temperature. Under these conditions, the number of strong hydrogen bonds is < 2-3 and there are > 4 weak hydrogen bonds, as observed in configurations of fluid extracted from each AIMD trajectory (Figure 2) and the statistical distribution of the strong, moderate and weak hydrogen bonds (Figure 3).

Compared to the OH stretching mode frequency of aqueous H_3BO_3 (at 3166 cm^{-1}) at ambient conditions given by Bezerra da Silva et al. (2018) and this study (the purple line in Figure 4), the OH stretching mode in intramolecular OH---O shows a red-shift with increasing temperature in supercritical fluids. This indicates a weakening of the intramolecular hydrogen bonds, in good agreement with the in-situ configuration snapshots (Figure 3). In addition, the other characteristic peaks (e.g. symmetric bending (δ-BO at ~503 cm^{-1}), out-of-plane bending (γ-BO at ~632 cm^{-1}), asymmetric stretching (ν_a-BO at ~1412 cm^{-1})) of H_3BO_3 split into several minor peaks. After evaluation of the individual vibrational modes (Figure A11), this splitting of characteristic peaks is attributed to decomposition of the vibration symmetry. Both the weakening of hydrogen bonds and the diversity in configurations of hydrated H_3BO_3 and $B(OH)_4^-$ in supercritical fluids contribute to the variation in vibrational frequencies, and induce a significant discrepancy in α_{3-4} compared to the AIMD under ambient conditions obtained by Rustad et al. (2010b).

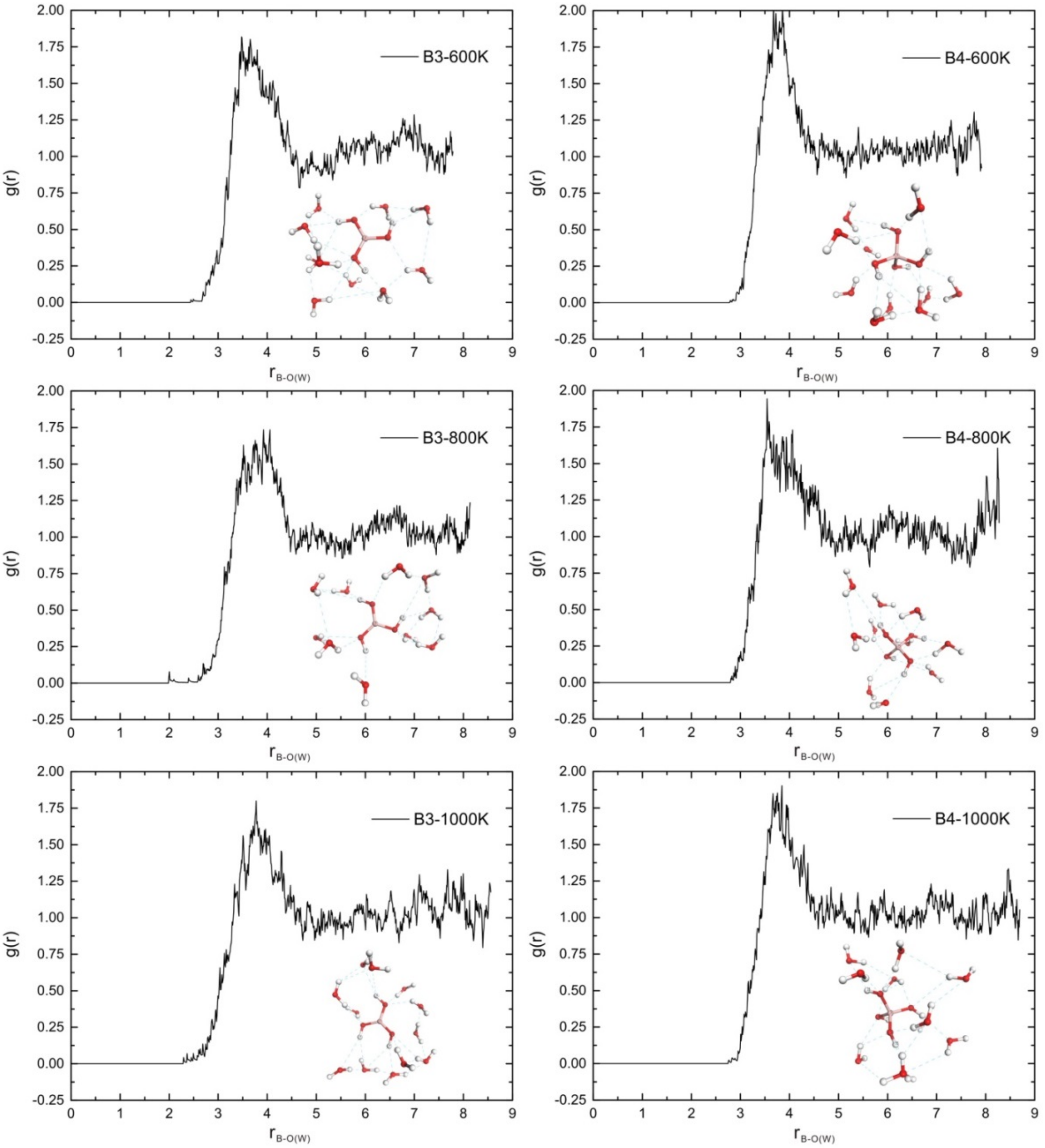

Figure 2. Radial distribution functions of aqueous H_3BO_3 (abbreviated as B3) and $B(OH)_4^-$ (abbreviated as B4) from the AIMD simulations of the supercritical fluids (i.e. 0.5 GPa, 600K, 800K, 1000K). Insets are in-situ snapshots of hydrated boron species.

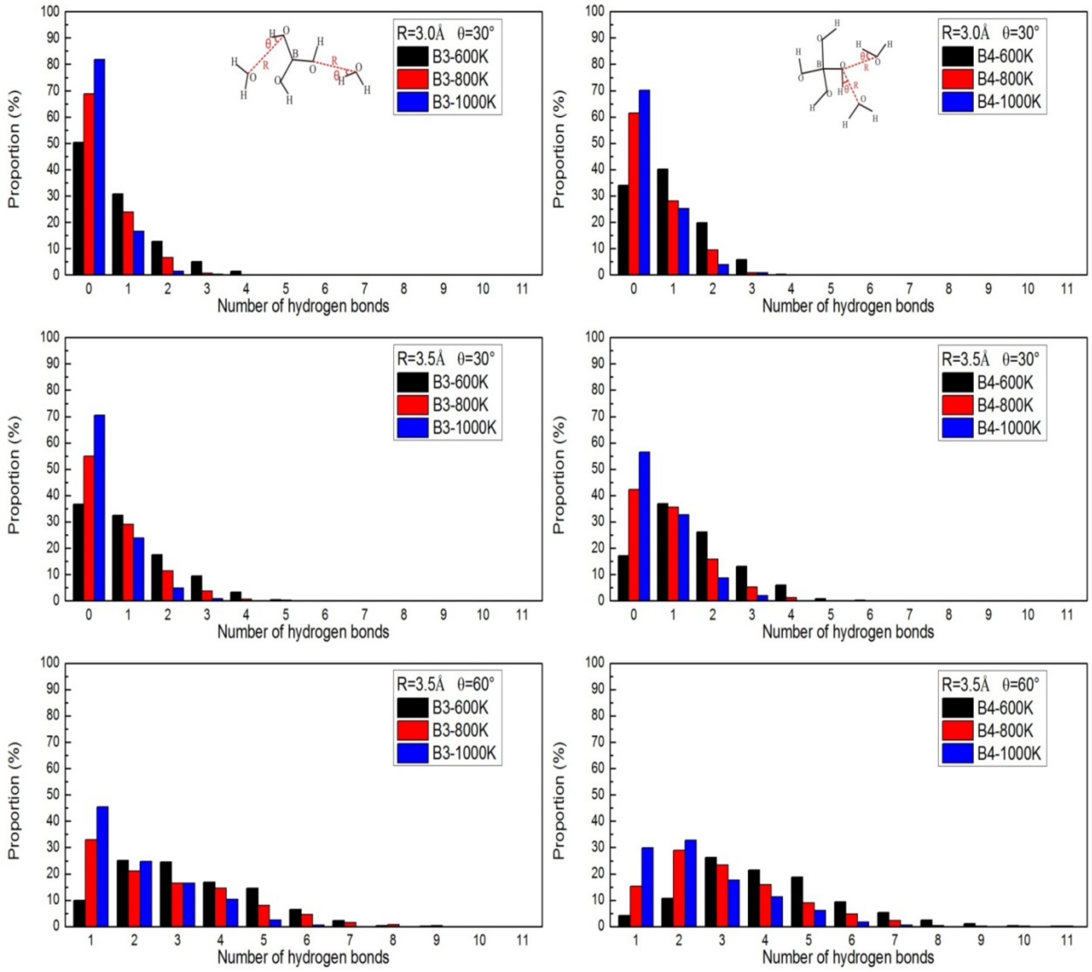

Figure 3. Histograms of the number of strong, moderate and weak hydrogen bonds of aqueous H_3BO_3 and $B(OH)_4^-$ in supercritical fluid. The statistics of hydrogen bonds were completed by the VMD program (Humphrey et al. 1996).

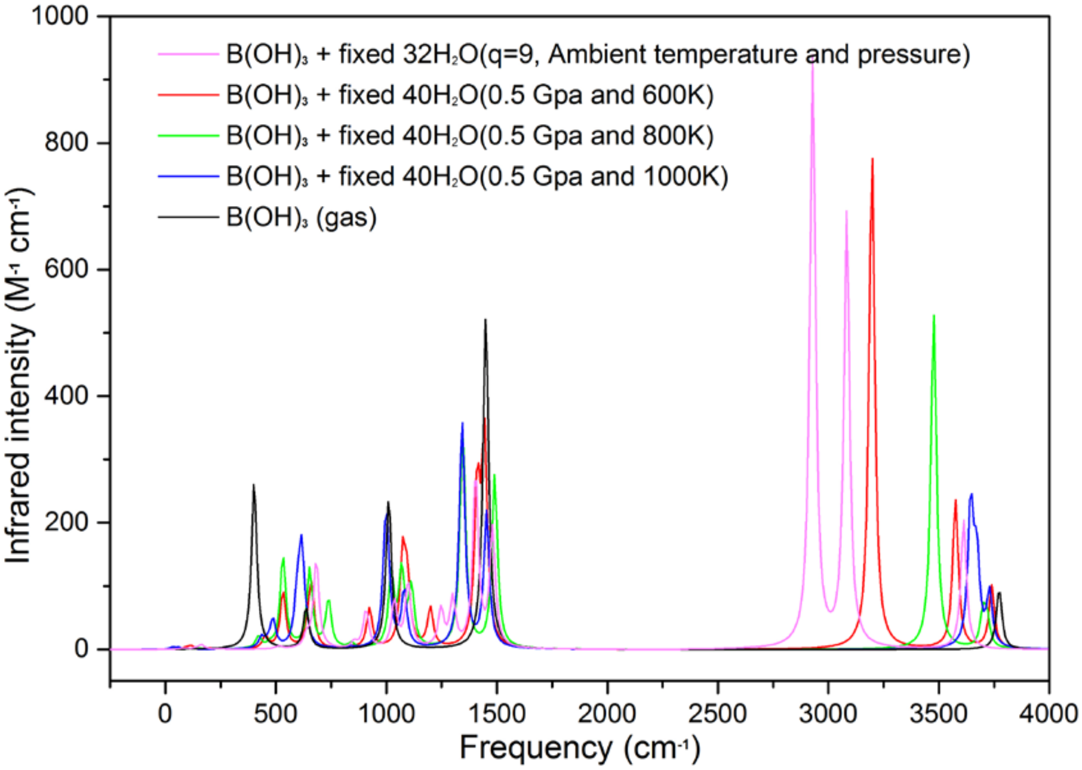

Figure 4. IR spectra of $H_3BO_3{\cdot}40H_2O$ at 0.5 GPa and 600 K, 800 K and 1000 K compared with the isolated and hydrated species at ambient conditions. Vibrational frequencies of $H_3BO_3{\cdot}40H_2O$ in supercritical fluid were calculated with individual configuration extracted from AIMD trajectories and only H_3BO_3 was relaxed with water molecules fixed in primitive high pressures/high temperature positions. At ambient condition, the frequencies of H_3BO_3+$32H_2O$ were calculated with fixing the surrounding water molecules. All calculations were completed with B3LYP/6-31G(d) combination.

4.2. Equilibrium fractionation of boron isotopes between tourmaline and supercritical aqueous fluid

Tourmaline is only stable at low pH, hence $B(OH)_4^-$ forms an insignificant portion of the total dissolved boron (Morgan and London, 1989). Studies of boron speciation in aqueous fluids at 22 to 600°C and 0.1 MPa to 2 GPa by Schmidt et al. (2005) concluded that high pressures stabilize $B(OH)_4^-$ relative to H_3BO_3, but the presence of significant amounts of $B(OH)_4^-$ can only be expected in relatively strong alkaline solutions, and the H_3BO_3 species remains the predominant boron species in the aqueous phase over a wide range of P-T-pH conditions (Schmidt et al., 2005). Experimental studies also indicate that the presence of trigonal boron coordination in slab fluids is a valid basic assumption in models of the fractionation of boron isotopes between the slab and fluid in subduction settings (Peacock and Hervig, 1999; Williams et al., 2001; Rosner et al., 2003). Hence, H_3BO_3 is considered to be the predominant boron species in supercritical fluid equilibrated with tourmaline in this study.

Boron isotope fractionations between dravite and fluids has been determined experimentally by Palmer et al. (1992) and Meyer et al. (2008). Both studies verified that no significant amount of tetrahedrally coordinated boron exists in dravite. The results of earlier theoretically and experimentally determined isotope fractionation factors between dravite and fluids ($1000\ln\alpha_{\text{Tur-fluid}}$) versus reciprocal temperatures are compared in Figure 5. As expected, all of the studies show that the extent of fractionation is inversely dependent on temperature. The temperature-dependent equilibrium fractionation of boron isotopes between dravite and fluid described by Meyer et al. (2008) yields $\Delta^{11}B_{(\text{Tur-fluid})} = -4.20\times1000/T+3.52$ ($R^2=0.77$) in the temperature range of 300-700°C with no pressure dependence observed under the condition of 200 MPa and 500 MPa conditions. In contrast, Palmer et al. (1992) concluded that the boron isotope fractionation factor is temperature and pressure dependent, with $\Delta^{11}B_{(\text{Tur-fluid})} = -5.82\times1000/T+3.27$ ($R^2=0.92$) at 200 MPa and $\Delta^{11}B_{(\text{Tur-fluid})} = -7.89\times1000/T+5.08$ ($R^2=0.97$) at 100 MPa. The theoretical temperature-dependent equilibrium fractionation of boron isotopes between dravite and fluid obtained from the multiple-methods gives $\Delta^{11}B_{(\text{Tur-fluid})} = -2.53\times1000/T+1.17$ ($R^2=0.96$), which is consistent with that obtained using an *ab initio* calculation approach (Kowalski et al., 2013), and also in good agreement with the experimental results of Meyer et al. (2008) that were determined using a $[B]_{\text{fluid}}/[B]_{\text{Tur}}$ value of 9.

The $\Delta^{11}B_{(tour-fluid)}$ values for the highest temperature for tourmaline formation observed in nature (i.e. 1023 K) are -0.618 ‰, -2.528 ‰ and -1.876 ‰ for the experimental studies by Meyer et al. (2008) and Palmer et al. (1992) and this theoretical study, respectively. More extensive boron isotope fractionation was observed at lower pressures by Palmer et al. (1992) (Figure 5), but they were uncertain whether the pressure effect resulted from equilibrium or kinetics processes. In contrast, the study by Meyer et al. (2008) observed no pressure dependence and attributed the apparent pressure effect to be a significant Rayleigh fractionation effect because of the small boron excess in the fluids in the experimental setup of Palmer et al. (1992) (i.e. $[B]_{fluid}/[B]_{tour}=0.1$). Indeed, it is possible that the steeper relationship between $1000\ln\alpha_{Tur-fluid}$ and temperature observed by Meyer et al. (2008) and calculated from this study may suggest a small degree of Rayleigh fractionation even in experiments with a relatively high $[B]_{fluid}/[B]_{tour}$.

In addition, smaller amounts of a four-coordinated boron species (B^{IV}) which may be attributed to dissolved metaboric acid HBO_2(aq) observed in neutral fluid by Schmidt et al. (2005). Kowalski et al. (2013) assumed at least 15-30% mole fraction of B^{IV} species compared to B^{III} species by integrating the peak areas of the Raman spectra given by Schmidt et al. (2005). If the contribution of B^{IV} species are taken into account, the theoretical lines are lifted and reach a good agreement with the experimental results of Meyer et al. (2008) at the high temperature range (~950 -1000 K) when there is ~10% B^{IV} species in the fluid (Figure 5). On the basis of this observation, we support the conclusion that the B^{IV} species is present in neutral fluid, as suggested by Raman spectra (Schmidt et al., 2005), boron isotope signatures (Meyer et al. 2008), and theoretical calculations (Kowalski et al. 2013)). Hence, both the contribution of B^{IV} in neutral fluid and an appropriate estimation of computational errors need to be included in theoretical predictions in this system.

In recent years, the effect of pressure on stable isotope fractionation has become a topic of considerable interest because of the potential for monitoring planetary differentiation. The potential pressure effect on equilibrium isotope fractionation is accounted by the changes in the molar volume as expressed in Eq. 7 (Young et al., 2015):

$$(\frac{\partial(10^3 ln\alpha)}{\partial P})_T = -\frac{10^3\Delta V}{RT} \quad \text{(Eq. 7)}$$

where V is the molar volume change associate with the isotope exchange reaction, and the effects can be significant at tens to hundreds of GPa and become potentially significant on planetary scales (Young et al., 2015).

The pressure dependence of the β factors of Li, and $B(OH)_3$ and $B(OH)_4^-$ in aqueous fluid have been systematically investigated by Kowalski and Jahn (2011) and Kowalski et al. (2013), indicating the β factors increase with increases in pressure, with good agreement with the frequency shifts measured experimentally by Sanchez-Valle et al. (2005). According to the relations of $1000(\beta-1) = 23.6 + 0.28P$ (GPa) for $B(OH)_3 \cdot 8H_2O$ and $1000(\beta-1) = 17.15 + 0.754P - 0.027P^2$ for $B(OH)_4^- \cdot 8H_2O$ fitted from the calculated values (Kowalski et al., 2013), the β values of 1.02374 and 1.01752 were derived at 1000 K and 0.5 GPa for aqueous $B(OH)_3$ and $B(OH)_4^-$, respectively. The resultant the $\alpha_{3\text{-}4}$ value of 1.0061, is in an excellent agreement with the $\alpha_{3\text{-}4}$ of 1.0055 ± 0.0004 from $H_3BO_3 \cdot 40H_2O$ and $B(OH)_4^- \cdot 40H_2O$ conformations extracted from AIMD trajectories under the same conditions using B3LYP/6-31G(d) in this study.

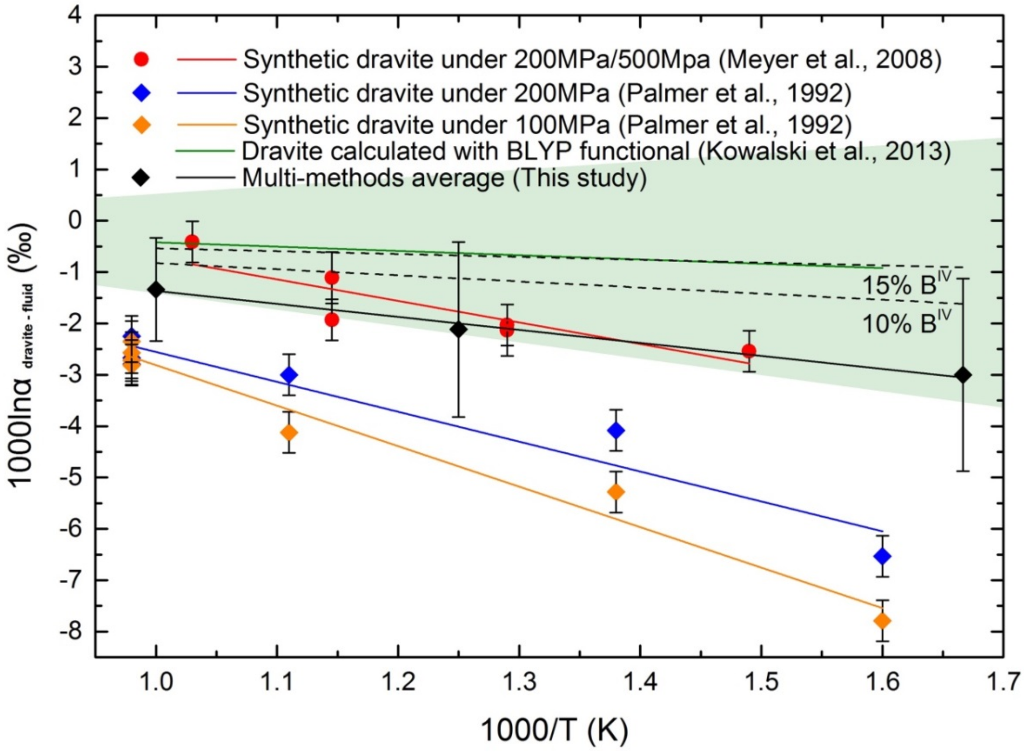

Figure 5. Comparison of theoretically and experimentally determined boron isotope fractionation 1000ln$\alpha_{\text{Tur-fluid}}$ versus reciprocal temperature between dravite and fluids under various conditions. The shadow area is the calculated error of Kowalski et al. (2013). The black diamonds and solid line represent our prediction for the boron isotope fractionation between dravite and acidic fluid containing only B^{III}. The black dash lines are our prediction for the boron isotope fractionation between dravite and neutral fluid containing 10% and 15% B^{IV}. The error bars in all data correspond to 2σ, and all data are fitted with linear regression.

4.3. Influence of chemical composition on equilibrium fractionation of boron isotopes among tourmaline group minerals

Large variations of $\delta^{11}B$ in tourmalines have been observed to correlate with their chemical compositions (i.e. higher $\delta^{11}B$ with higher concentrations of Fe), leading to suggestions that boron isotope fractionation during tourmaline formation is chemistry dependent to some degree

(Chaussidon and Albarede, 1992; Tonarini et al., 1998). Equilibrium fractionation of stable isotopes is mainly controlled by the relevant bond strengths. For example, Wang et al. (2017) showed that the Mg-Ca concentration in carbonate minerals affects the Mg-Ca isotope equilibrium fractionation by varying the Ca-O and Mg-O bond lengths, and hence the bond strength and vibrational frequency. Because the tourmaline crystal structure is also composition-dependent (Fortier and Donnay, 1975), the influences of chemical compositions on the $\alpha_{\text{Tur-fluid}}$ are quantified here. This quantification includes comparison of Mg-foitite and dravite, and dravite and schorl solid solutions. The Mg-foitite model was constructed by replacing the composition of dravite according to the exchange vector of □Al(NaMg)$_{-1}$, (where □ is a vacancy). The calculation suggests that the equilibrium boron isotope fractionation of dravite is slightly greater than that within Mg-foitite, such that $1000\ln\alpha_{\text{Tur-fluid}}$ between Mg-foitite and dravite varies between +0.17‰ and +0.36‰ over the temperature range 600 to 1000 K (Figure 6). Experimental $\Delta^{11}B_{(\text{Tur-fluid})}$ values of synthesized dravite consisting of 2/3 dravite and 1/3 Mg-foitite by following Meyer et al. (2008) show a large negative deviation from the equilibrium lines of both pure dravite and pure Mg-foitite. Because these tourmaline samples were synthesized under conditions with only a small boron excess in the fluid (i.e. $[B]_{\text{fluid}}/[B]_{\text{tour}} = 0.1$), the large apparent fractionation of up to -4.7‰ is likely due to Rayleigh fractionation, as stressed by Meyer et al. (2008).

There is a wide variety of tourmalines in nature, so a series of solid solution models were constructed individually. As shown in Figure 6, the equilibrium boron isotope fractionation lines of the two tourmaline solid solutions dravite+Fe and schorl+Mg, fall between the end-member tourmalines of dravite and schorl, and the $1000\ln\alpha_{\text{Tur-fluid}}$ of tourmaline become greater with increasing Mg/(Fe+Mg) ratios within the solid solution. Similar equilibrium boron isotope fractionations were observed between hydroxy-liddicoatite and Mg-foitite, as well as between olenite and schorl, indicating that occupation of the Mg, Fe, and Al at the *Y* sites dominates the chemistry dependent equilibrium fractionation of boron isotopes during tourmaline crystallization.

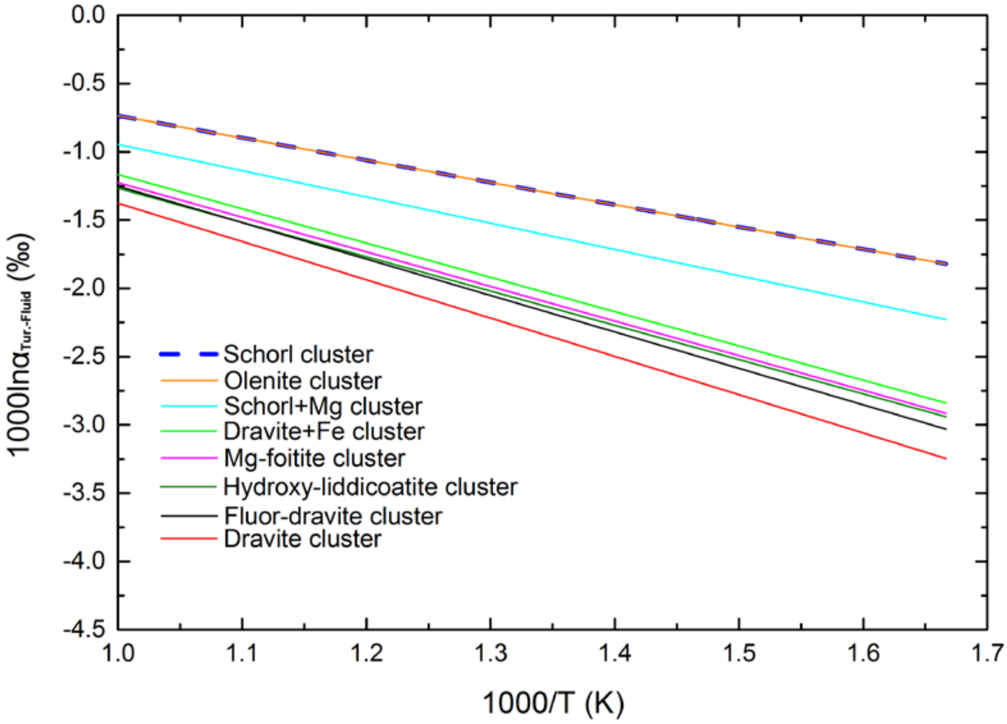

Figure 6. Comparison of equilibrium boron isotope fractionation of tourmaline with different composition. All models optimized with B3LYP/6-31G(d). The overall errors in $\Delta^{11}B_{(tour-fluid)}$ were estimated to be ± 1.9‰, ± 1.7‰ and ± 1.0‰ at 600 K, 800 K and 1000 K, and are similar to those obtained by Kowalski et al. (2013). The chemical compositions of the tourmaline group represented here are: Dravite: $NaMg_3Al_6[Si_6O_{18}][BO_3]_3(OH)_4$; Mg-foitite: $Mg_2AlAl_6[Si_6O_{18}][BO_3]_3(OH)_4$; Dravite+Fe: $Na(Mg_2Fe)Al_6[Si_6O_{18}][BO_3]_3(OH)_4$; Olenite: $NaAl_3Al_6[Si_6O_{18}][BO_3]_3O_3(OH)$; Fluor-dravite: $NaMg_3Al_6[Si_6O_{18}][BO_3]_3(OH)_3F$; Schorl: $NaFe_3Al_6[Si_6O_{18}][BO_3]_3(OH)_4$; Schorl+Mg: $Na(Fe_2Mg)Al_6[Si_6O_{18}][BO_3]_3(OH)_4$; Hydroxy-liddicoatite: $CaMgLi_2Al_6[Si_6O_{18}][BO_3]_3(OH)_4$.

4.4. Driving mechanism of equilibrium boron isotope fractionation between tourmalines and fluid

4.4.1. B-O bond length

At equilibrium, boron isotopic fractionation between tourmaline and fluid may reflect second order effects; such as, differences in bond lengths, geometries, energies and electronic environments of the trigonal planar BO_3-groups in tourmaline and fluids, in addition to the first order thermodynamic effects (*P-T*) of tourmaline crystallization. At high temperatures (i.e. T >> 300 K), Bigeleisen & Mayer (1947) proposed an approximate expression to compute fractionation factors as follow:

$$\alpha_{\text{A-B}} \approx 1 + \frac{\Delta m}{m^2} \frac{h^2 (F_A - F_B)}{96\pi^2 k^2 T^2} \qquad \text{(Eq. 8)}$$

where *m* represents the atomic mass of the element being investigated; *Δm*, the difference in the mass for the isotopes of interest; *h* is Plank's constant; *k* is Boltzmann's constant and *T* is the temperature in degrees Kelvin; F_A, the sum of the bond force constants for substance *A* that oppose displacement of the atom of interest in each of three perpendicular directions; and F_B, the corresponding sum of force constants for substance *B*.

The variation of $1000\ln\alpha_{\text{Tur-fluid}}$ vs. average B-O bond lengths is illustrated in Figure 7, and shows that the boron isotope fractionation ($1000\ln\alpha_{\text{Tur-fluid}}$) increases linearly with the increase of the average B-O bond length of tourmaline (Table 1). In the case of the tourmaline group minerals, the average B-O bond length of tourmaline increases with increasing Mg content in the solid solution, indicating that the occupation of Mg at *Y* sites enlarges the B-O bond length and induces a larger boron isotope fractionations between minerals and fluid (Figure 7ab). In contrast, the occupation of *Y* sites by Al atoms in olenite shortens the B-O bond length and results in smaller $1000\ln\alpha_{\text{Tur-fluid}}$ values than in dravite. The linear trend, including gaseous and aqueous boron species, has been reported in previous work by Kowalski et al. (2013). The B-O bond lengths of 1.378 Å for olenite and 1.397 Å for dravite by Kowalski et al. (2013) are consistent with these of 1.375 Å and 1.382 Å from this study (Table 1). Similar dependences on bond length have been observed in Sr isotope fractionations among Sr-substituted minerals

(Widanagamage et al., 2014), Si isotope fractionations in silicates (Méheut et al., 2014), and Li isotope fractionations in aqueous Li species (Kowalski and Jahn, 2011). However, it is not universally applicable, for example, Mg isotope fractionation is insensitive to changes in the Mg-O bond length in mantle minerals (e.g., forsterite, orthoenstatite, diopside) (Schauble, 2011).

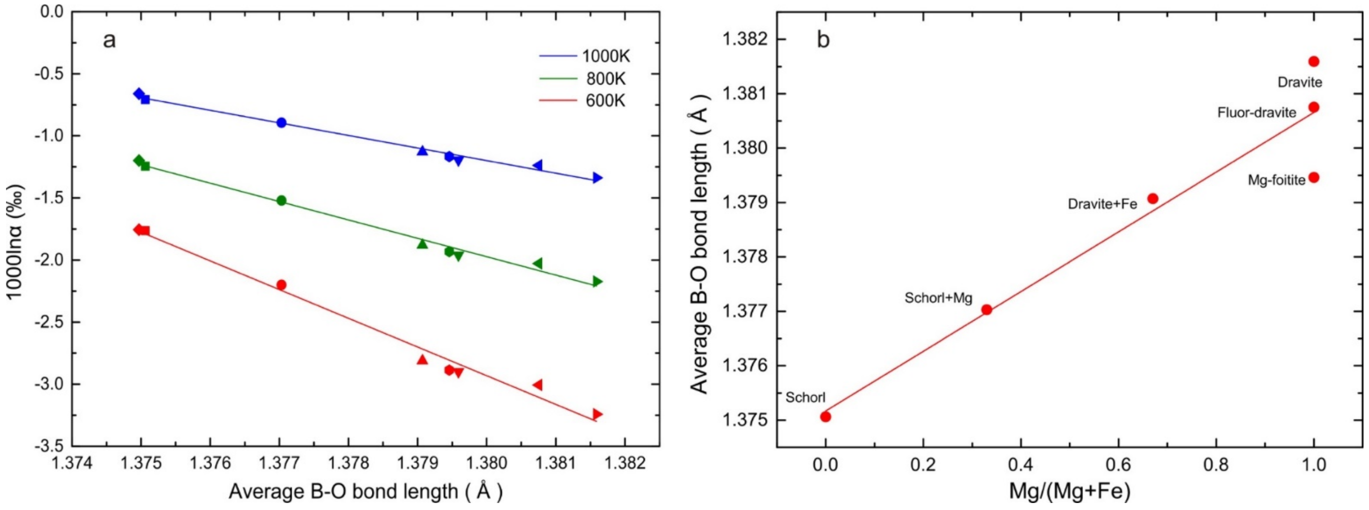

Figure 7. (a) Dependence of $1000\ln\alpha_{\text{Tur-fluid}}$ on the average B-O bond lengths in tourmaline group minerals at 1000 K, 800 K and 600 K; (b) Dependence of the B-O bond length on the Mg content in solid solution.

Table 1. Dependence of $1000\ln\alpha_{\text{tour-fluid}}$ on the average B-O bond length in different tourmalines

Model	Average B-O bond length (Å)	$1000\ln\alpha_{\text{Tur-fluid}}$ (‰)			Gibbs free energy ^{a} ($\times10^{7}$ kcal/mol)
		1000 K	800K	600 K	
Schorl	1.37506	-1.3274	-1.1231	-2.7559	-3.67
Schorl+Mg	1.37703	-1.5153	-1.3994	-3.1929	-3.39
Dravite+Fe	1.37907	-1.7120	-1.6887	-3.6534	-3.11
Hydroxy-liddicoatite	1.37959	-1.8146	-1.8406	-3.8930	-2.88
Olenite	1.37497	-1.2814	-1.0771	-2.7489	-2.87
Fluor-dravite	1.38075	-1.24	-2.03	-3.01	-2.84
Dravite	1.38159	-1.9579	-2.0529	-4.2346	-2.84
Mg-foitite	1.37946	-1.7880	-1.8112	-3.8783	-2.83

[a]: The Gibbs free energy were calculated with B3LYP/6-31G(d) under 1 *atm* and 298.15 K.

4.4.2. Mass to charge ratios of total metal atoms in X, Y and Z sites of tourmaline

As noted, there is empirical evidence that the δ^{11}B value of tourmaline is dependent on its chemical composition (Chaussidon and Albarede, 1992; Lambert-Smith et al., 2016). In this context, the key parameter is the mass/charge ratios of cations in the octahedral site (Figure A8), namely Mg^{2+}, Fe^{2+}, Li^+ and Al^{3+} etc. In addition to local chemical interactions, the variable chemical composition can affect the isotope fractionation properties of a solid solution by changes in cell parameters and relevant molar volumes. For example, the occupation of Mg^{2+} (Fe^{2+}) in *Y* sites of tourmaline induces variations in the cell parameters (Table A10). The dependence of the boron isotope fractionation on the sum of products of metal ion radius and apparent charge in *X*, *Y* and *Z* sites of tourmaline (i.e. *S*) using the parameters listed in Table 2 and illustrated in Figure 8. There are positive linear correlations between $1000\ln\alpha_{\text{Tur-fluid}}$ with *S* at 1000 K, 800 K and 600 K (Figure 8a), and with the mass to charge ratios (*M/E*) at 600 K in a series of schorl-dravite solid solutions (Figure 8b). Note, the Mg-foitite and hydroxyl-liddicoatite solid solutions with similar M/E ratios have identical $1000\ln\alpha_{\text{Tur-fluid}}$ values, indicating that the *M/E* ratio plays a role in defining the boron isotopic variability of natural tourmalines. Indeed, a recent study verified that the relationship between metal ions in the *X* site and the boron isotope composition of tourmaline can be used to distinguish ore-forming fluids (Lambert-Smith et al., 2016).

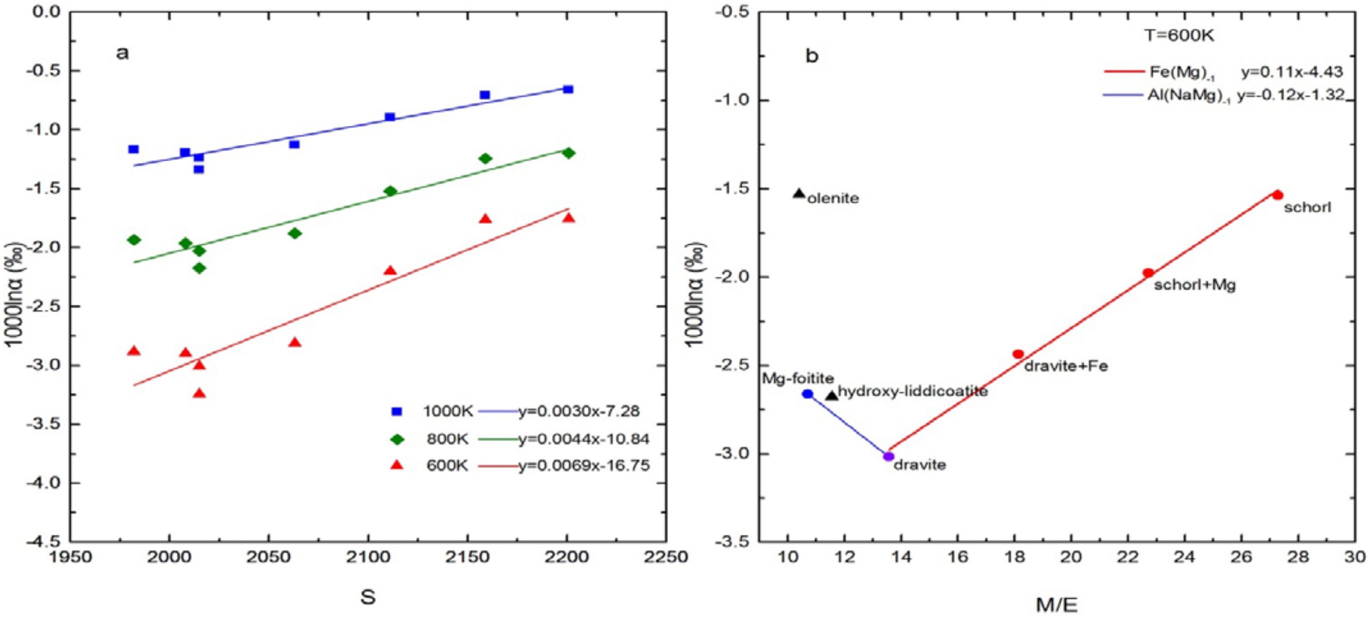

Figure 8. Relationship of boron isotope fractionation between tourmalines and fluids with *S* at 1000 K, 800 K and 600 K (a), and with the *M/E* ratios at 600 K (b). *S* is the sum of products of metal ion radius and apparent charge in *X* and *Y* sites of the tourmaline. M and E, respectively, are the atomic weights and the apparent charge of metal atoms in *X* and *Y* sites of the tourmaline models. The metal ion radii and atomic weights of metals at sites of *X*, *Y*, *Z* are from Ignatiev (2005) and Coplen (2001).

Table 2. Dependence of $1000\ln\alpha_{\text{Tur-fluid}}$ on the sum of products of metal ion radius and apparent charge in *X*, *Y* and *Z* sites of tourmaline

Model	**Sites**			***S***
	X	***Y***	***Z***	
schorl	Na^+	$3Fe^{2+}$	$6Al^{3+}$	2159
olenite	Na^+	$3Al^{3+}$	$6Al^{3+}$	2201
schorl+Mg	Na^+	$2Fe^{2+}$, Mg^{2+}	$6Al^{3+}$	2111
dravite+Fe	Na^+	$2Mg^{2+}$, Fe^{2+}	$6Al^{3+}$	2063
hydroxy-liddicoatite	Ca^{2+}	$2Li^+$, Al^{3+}	$6Al^{3+}$	2008
Mg-foitite	□	$2Mg^{2+}$, Al^{3+}	$6Al^{3+}$	1982
dravite (Fluor-dravite)	Na^+	$3Mg^{2+}$	$6Al^{3+}$	2015

*Data for metal ion radii and atomic weights of metals at sites of X, Y, Z are from Ignatiev (2005) and Coplen (2001).

4.5. Crystallization sequence

The Gibbs free energies of tourmaline formation ($\Delta G_{formation}$) were calculated from each cluster model in the solid solution series of tourmalines by B3LYP/6-31G(d)) at 1 atm and 298.15 K. Consequently, the general crystallization sequences of a zoned tourmaline from core to rim is predicted to be schorl, schorl+Mg, dravite+Fe, hydroxyl-liddicoatite, olenite, dravite and Mg-foitite (Figure 9), in the absence of chemical availability constraints in the fluid phase and under constant P-T conditions. As the prediction is purely theoretical, it applies if the tourmaline is crystallizing from a batch of fluid which has an excess of all the constituents of tourmaline except for Fe and Mg. In this case, schorl will precipitate first and, as the fluid becomes relatively depleted in Fe the tourmaline will become progressively more Mg-rich. This is consistent with the chemical compositions observed in natural occurring zoned tourmaline minerals, such as those from ore deposits in the eastern Qinling mountains, E. China (Jiang et al., 1995; Xue et al., 1997), showing higher Fe contents in their cores and Mg enrichment in their rims. The same pattern is found in pegmatitic tourmalines from the Moldanubian zone (Czech Republic) with a decrease in Fe/(Fe+Mg) ratios from the core to intermediate zone and outer rims (Gadas et al., 2012). When combined with the calculated boron isotope fractionation factors among tourmaline group minerals (Figure 6), this may account for the association of boron isotope zonation with chemical zonation in tourmaline grains that have lower δ^{11}B and higher Mg/(Mg+Fe) values in the rims relative to the cores (e.g., Marschall and Foster, 2018). However, there are many examples of tourmaline from ore deposits that show evidence of changing fluid compositions and temperature over the course of tourmaline formation. Indeed, there are many examples of reversals in zoning patterns during tourmaline formation (e.g., Jiang et al., 1998).

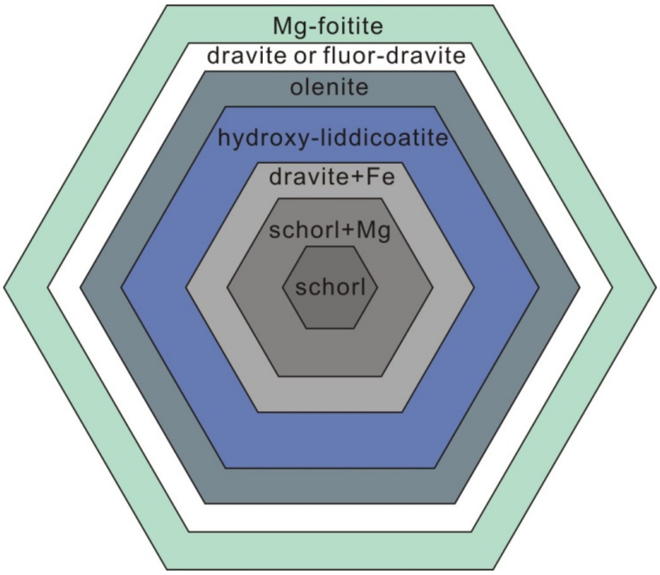

Figure 9. Crystallization sequence of seven tourmalines according to the Gibbs free energy of formation calculated with B3LYP/6-31G(d). From core to rim, the individual colors represent schorl, schorl+Mg, dravite+Fe, hydroxy-liddicoatite, olenite, dravite (or fluor-dravite) and Mg-foitite respectively.

4.6. Wider Implications

Tourmalines from mineral deposits, metamorphic environments and igneous complexes frequently display complex chemical and isotopic zoning patterns that reflect the combinations of changes in physical conditions, chemical evolution of fluids, Rayleigh fractionation effects, and equilibration with co-existing mineral phases (e.g., Henry, 1996; Jiang et al., 1998, 2001; Siegel et al., 2016). Zoning patterns may also be unidirectional or oscillatory, with examples of both types occurring in the same deposit (e.g., Jolliff et al., 1986; Henry, 1996; Jiang et al., 1998). It is, therefore, difficult to ascribe observed patterns in the chemical and boron isotopic composition of specific tourmaline occurrences to individual processes. The situation is even more complex in pegmatitic tourmalines, where debate remains concerning the relative importance of silicate-melt versus high-temperature silica-rich aqueous fluids in the crystallization/precipitation of tourmaline, and for which the tourmaline-melt and tourmaline-fluid boron isotope fractionation factors have an opposite sense (Siegel et al., 2016). Nevertheless, the temperature and chemistry dependence of boron isotope fractionation ($1000\ln\alpha_{\text{Tur-fluid}}$) that have been identified and quantified in this study provide constraints on the interpretation of covariations in tourmaline chemical and isotopic compositions.

In some cases, the impact of tourmaline chemistry on δ^{11}B values is relatively small. For example, in a study of Catalina metasediments, Bebout and Nakamura (2003) documented a concomitant decrease in the Fe/(Fe+Mg) ratio from 0.28 to 0.18 and the δ^{11}B value from -7 ‰ to -14 ‰ in tourmaline precipitated from fluids during prograde metamorphism at epidote-amphibolite grades (~400°C). From the temperature-($1000\ln\alpha_{\text{Tur-fluid}}$) relationships illustrated in Figure 6, it can be calculated that only 0.14 ‰ instead of the 7 ‰ decrease in δ^{11}B values arose from the change in tourmaline chemistry.

However, at lower temperatures and in environments where there is a wider range in tourmaline chemistry, the consequences of the different relationships illustrated in Figure 6 and Figure 9 become more significant. For example, Slack (1996) summarized the typical chemistries of hydrothermally precipitated tourmaline from 14 different settings and observed Fe/(Fe+Mg) ratios ranging between 0.149 and 0.806. The boron isotope fractionation-temperature relationship determined by Meyer et al. (2008) yields a ($1000\ln\alpha_{\text{Tur-fluid}}$) value of -3.26 ‰ at a typical hydrothermal temperature of 350°C. This compares to values of -2.65 ‰ and -1.74 ‰ for the most Mg-rich and Fe-rich tourmalines, respectively, identified by Slack (1996) using the relationships shown in Figure 6. Alternatively, if ($1000\ln\alpha_{\text{Tur-fluid}}$) is known for a particular system, its formation temperature can be calculated. For example, if ($1000\ln\alpha_{\text{Tur-fluid}}$) is -2.5 ‰, the Meyer et al. (2008) relationship yields a tourmaline precipitation temperature of 429°C, compared to 378°C (Fe/(Fe+Mg) = 0.149) and 185°C (Fe/(Fe+Mg) = 0.806), calculated using the relationships determined in this study. While there are other processes that play an important role in defining the δ^{11}B values of hydrothermally precipitated tourmaline (as discussed above), it is therefore apparent that the chemical composition of the tourmaline must be taken in account when its boron isotopic composition is used to reconstruct past environmental conditions.

CONCLUSIONS

The temperature-dependent boron isotope fractionation between tourmaline group minerals and fluid was investigated by density functional theory calculations. The *ab initio* molecular dynamics (AIMD) were carried out to understand the dynamic effects on the isotope fractionation in supercritical fluid. The evidence presented above leads to the following general conclusions in this study:

i) the first solvent shell controls the boron isotope fractionation in solution, where the β factors of hydrated H_3BO_3 and $B(OH)_4^-$ decrease with increasing numbers of hydrogen bonds;

ii) in the supercritical fluids (i.e. 0.5 GPa, 600-1000K), the first solvent shell becomes less distinct with increasing temperature, and the weakening of hydrogen bonds and the diversity in configurations of hydrated H_3BO_3 and $B(OH)_4^-$ induces a significant change in α_{3-4} compared to the ambient conditions;

iii) the $1000\ln\alpha_{\text{Tur-fluid}}$ value increases with increasing Mg/(Fe+Mg) ratios in a series of dravite-schorl solid solutions and, in combination with the crystallization sequence, it describes the association of boron isotope zonation with chemical zonation observed in zoned tourmaline grains;

iv) the chemical composition of tourmalines plays an important role in controlling the extent of boron isotope fractionation between tourmaline and fluids. This effect is likely the most important in tourmalines crystallized from relatively low-temperature hydrothermal systems that commonly display wide ranges in both $\delta^{11}B$ values and chemical composition.

Acknowledgements:

This research was supported by the National Natural Science Foundations of China (Grants Nos. 41973005, 41673001, 41830428, 21673111). We are grateful to Prof. Méheut and Prof. Kowalski for their valuable scientific comments, and to the High Performance Computing Center (HPCC) of Nanjing University for doing the numerical calculations in this paper for its blade cluster system.

Appendix A. Supplementary data associated with this article can be found, in the online version.

REFERENCES

Bebout, G. E. and Nakamura, E., 2003. Record in metamorphic tourmalines of subduction-zone devolatilization and boron cycling. Geology 31, 407-410.

Bezerra da Silva M., Santos R.C.R., Freire P.T.C., Caetano E.W.S., Freire V.N., 2018. Vibrational Properties of Bulk Boric Acid 2A and 3T Polymorphs and Their Two-Dimensional Layers: Measurements and Density Functional Theory Calculations. J. Phys. Chem. A. 122, 1312−1325.

Bigeleisen, J., Mayer, M. G., 1947. Calculation of equilibrium constants for isotopic exchange reactions. J. Chem. Phys. 15, 261-267.

Blanchard, M., Poitrasson, F., Méheut, M., Lazzeri, M., Mauri, F., Balan, E., 2009. Iron isotope fractionation between pyrite (FeS_2), hematite (Fe_2O_3) and siderite ($FeCO_3$): A first-principles density functional theory study. Geochim. Cosmochim. Acta. 73, 6565-6578.

Blanchard, M., Poitrasson, F., Méheut, M., Lazzeri, M., Mauri, F., Balan, E., 2012. Comment on “New data on equilibrium iron isotope fractionation among sulfides: Constraints on mechanisms of sulfide formation in hydrothermal and igneous systems" by V.B. Polyakov and D.M. Soultanov. Geochim. Cosmochim. Acta. 87, 356-359.

Bosi, F., Andreozzi, G. B., Federico, M., Graziani, G., Lucchesi, S., 2005. Crystal chemistry of the elbaite-schorl series. Am. Mineral. 90, 1784-1792.

Chaussidon, M., Albarède, F., 1992. Secular boron isotope variations in the continental crust: an ion microprobe study. Earth Planet. Sci. Lett. 108, 229-241.

Coplen, T. B., 2001. Atomic Weights of the Elements 1999. J. Phys. Chem. Ref. Data. 30, 701-712.

Dupuis, R., Benoit, M., Nardin, E. and Méheut, M., 2015. Fractionation of silicon isotopes in liquids: the importance of configurational disorder. Chem. Geol. 396, 239-254.

Felmy, A. R., Weare J. H., 1986. The prediction of borate mineral equilibria in natural waters: Application to Searles Lake, California. Geochim. Cosmochim. Acta. 50, 2771-2783.

Fortier, S., Donnay, G., 1975. Schorl refinement showing composition dependence of the tourmaline structure. Can. Mineral. 13, 173-177.

Frisch, M. J., Trucks, G. W., Schlegel, H. B., Scuseria, G. E., Robb, M. A., Cheeseman, J. R., Scalmani, G., Barone, V., Petersson, G. A., Nakatsuji, H., Li X., Caricato, M., Marenich, A. V., Bloino, J., Janesko, B. G., Gomperts, R., Mennucci, B., Hratchian, H. P., Ortiz, J. V., Izmaylov, A. F., Sonnenberg, J. L., Williams Ding, F., Lipparini, F., Egidi, F., Goings, J., Peng, B., Petrone, A., Henderson, T., Ranasinghe, D., Zakrzewski, V.G., Gao, J., Rega, N., Zheng, G., Liang, W., Hada, M., Ehara, M., Toyota, K., Fukuda, R., Hasegawa, J., Ishida, M., Nakajima, T., Honda, Y., Kitao, O., Nakai, H., Vreven, T., Throssell, K., Montgomery, Jr., J A., Peralta, J. E., Ogliaro, F., Bearpark, M. J., Heyd, J. J., Brothers, E. N., Kudin, K. N., Staroverov, V. N., Keith, T. A., Kobayashi, R., Normand, J., Raghavachari, K., Rendell, A. P., Burant, J. C., Iyengar, S. S., Tomasi, J., Cossi, M., Millam, J. M., Klene, M., Adamo, C., Cammi, R., Ochterski, J. W., Martin, R. L., Morokuma, K., Farkas, O., Foresman, J. B., Fox, D. J., 2016. *Gaussian 16, Wallingford, CT.*

Gadas, P., Novák, M., Staněk, J., Filip, J., Vašinová Galiová, M., 2012. Compositional evolution of zoned tourmaline crystals from pockets in common pegmatites of the Moldanubian Zone. Czech Republic. Can. Mineral. 50, 895-912.

Gao, C. H., Cao, X. B., Liu, Q., Yang, Y. H., Zhang, S. T., He, Y. Y., Tang, M., Liu, Y., 2018. Theoretical calculation of equilibrium Mg isotope fractionations between minerals and aqueous solutions. Chem. Geol. 488, 62-75.

Gibbs, G., 1982. Molecules as models for bonding in silicates. Am. Mineral. 67, 421-450.

Grimme, S., 2006. Semiempirical GGA-type density functional constructed with a long-range dispersion correction. J. Comput. Chem. 27, 1787-1799.

Henry, D. J., Dutrow, B. L., 1996. Metamorphic tourmaline and its petrologic applications. Rev. Mineral. 33, 503-557.

Henry, D. J., Dutrow, B. L., 2012. Tourmaline at diagenetic to low-grade metamorphic conditions: Its petrologic applicability. Lithos. 154, 16-32.

Henry, D. J., Guidotti, C. V., 1985. Tourmaline as a petrogenetic indicator mineral- An example from the staurolite-grade metapelites of NW Maine. Am. Mineral. 70, 1-15.

Huang, F., Chen, L., Wu, Z., Wang, W., 2013. First-principles calculations of equilibrium Mg isotope fractionations between garnet, clinopyroxene, orthopyroxene, and olivine: Implications for Mg isotope thermometry. Earth Planet. Sci. Lett. 367, 61-70.

Huang, F., Wu, Z., Huang, S., Wu, F., 2014. First-principles calculations of equilibrium silicon isotope fractionation among mantle minerals. Geochim. Cosmochim. Acta. 140, 509-520.

Humphrey, W., Dalke, A., Schulten, K., 1996. VMD: visual molecular dynamics. J. Mol. Graph. 14, 33-38.

Ignatiev, V.D., 2005. Sizes of atoms and ions and covalency of bonding in molecules and crystals. J. Struct. Chem. 46, 744-751.

Jahn, S. and Wunder, B., 2009. Lithium speciation in aqueous fluids at high P and T studied by ab initio molecular dynamics and consequences for Li-isotope fractionation between minerals and fluids. Geochim. Cosmochim. Acta. 73, 5428-5434.

Jiang, S. Y., Palmer, M. R., Li, Y. H., Xue, C. J., 1995. Chemical compositions of tourmaline in the Yindongzi-Tongmugou Pb-Zn deposits, Qinling, China: Implications for hydrothermal ore-forming processes. Miner. Deposita. 30, 225-234.

Jiang, S. Y., Palmer, M. R., Slack, J. F., Shaw, D. R., 1998. Paragenesis and chemistry of multistage tourmaline formation in the Sullivan Pb-Zn-Ag deposit, British Columbia. *Econ. Geol.* **93**, 47-67.

Jiang, S. Y., 2001. Boron isotope geochemistry of hydrothermal ore deposits in China: a preliminary study. Phys. Chem. Earth Part A. 26, 851-858.

Jiang, S. Y., Slack, J. F., Palmer, M. R., 2000. Sm-Nd dating of the giant Sullivan Pb-Zn-Ag deposit, British Columbia. Geology. 28, 751-754.

Jolliff, B. L., Papike, J. J., Shearer, C. K., 1986. Tourmaline as a recorder of pegmatite evolution: Bob Ingersoll pegmatite, Black Hills, South Dakota. Am. Mineral. 71, 472-500.

Klochko, K., Kaufman, A. J., Yao, W., Byrne, R. H., Tossell, J. A., 2006. Experimental measurement of boron isotope fractionation in seawater. Earth Planet. Sci. Lett. 248, 276-285.

Kowalski, P. M., Jahn, S., 2011. Prediction of equilibrium Li isotope fractionation between minerals and aqueous solutions at high P and T: an efficient ab initio approach. Geochim. Cosmochim. Acta. 75, 6112-6123.

Kowalski, P. M., Wunder, B., Jahn, S., 2013. Ab initio prediction of equilibrium boron isotope fractionation between minerals and aqueous fluids at high P and T. Geochim. Cosmochim. Acta. 101, 285-301.

Kowalski, P.M., Wunder, B., 2018. Boron Isotope Fractionation Among Vapor–Liquids–Solids–Melts: Experiments and Atomistic Modeling, in: Marschall, H., Foster, G. (Eds.), Boron Isotopes: The Fifth Element. Springer International Publishing, Cham, pp. 33-69.

Krienitz, M. S., Trumbull, R., Hellmann, A., Kolb, J., Meyer, F., Wiedenbeck, M., 2008. Hydrothermal gold mineralization at the Hira Buddini gold mine, India: constraints on fluid evolution and fluid sources from boron isotopic compositions of tourmaline. Miner. Deposita. 43, 421-434.

Kubicki, J.D., 2001. Self-Consistent Reaction Field Calculations of Aqueous Al^{3+}, Fe^{3+}, and Si^{4+}: Calculated Aqueous-Phase Deprotonation Energies Correlated with Experimental ln(Ka) and pKa. J. Phys. Chem. A. 105, 8756-8762.

Lambert-Smith, J. S., Rocholl, A., Treloar, P. J., Lawrence, D. M., 2016. Discriminating fluid source regions in orogenic gold deposits using B-isotopes. Geochim. Cosmochim. Acta. 194, 57-76.

Liebscher, A., Meixner, A., Romer, R., Heinrich, W., 2005. Liquid-vapor fractionation of boron and boron isotopes: Experimental calibration at 400 ^{0}C/23 MPa to 450 ^{0}C /42 MPa. Geochim. Cosmochim. Acta. 69, 5693-5704.

Li, X. F., Zhao, H., Tang, M., Liu, Y., 2009. Theoretical prediction for several important equilibrium Ge isotope fractionation factors and geological implications. Earth Planet. Sci. Lett. 287 (1-2), 1-11.

Li, X. F., Liu Y., 2010. First-principles study of Ge isotope fractionation during adsorption onto Fe(III)-oxyhydroxide surfaces. Chem. Geol. 278 (1-2), 15-22.

Li, X. F., Liu, Y., 2011. Equilibrium Se isotope fractionation parameters: a first-principles study. Earth Planet. Sci. Lett. 304 (1-2), 113-120.

Li, X. F., Liu, Y., 2015. A theoretical model of isotopic fractionation by thermal diffusion and its implementation on silicate melts. Geochim. Cosmochim. Acta. 154, 18-27.

Liu, Y. and Tossell, J. A., 2005. Ab initio molecular orbital calculations for boron isotope fractionations on boric acids and borates. Geochim. Cosmochim. Acta. 69, 3995-4006.

Marschall, H. R. and Foster, G. L., 2018. Advances in Isotope Geochemistry: Boron Isotopes The Fifth element. Springer.

Marschall, H. R., Jiang, S. Y., 2011. Tourmaline Isotopes: No Element Left Behind. Elements. 7, 313-319.

McQuarrie, D.A., Donald, A., 1973. Statistical thermodynamics. New York, NY. Harper and Row, pp. 356.

Méheut, M., Lazzeri, M., Balan, E. and Mauri, F., 2007. Equilibrium isotopic fractionation in the kaolinite, quartz, water system: Prediction from first-principles density-functional theory. Geochim. Cosmochim. Acta. 71, 3170-3181.

Méheut, M., Lazzeri, M., Balan, E., Mauri, F., 2009. Structural control over equilibrium silicon and oxygen isotopic fractionation: A first-principles density-functional theory study. Chem. Geol. 258, 28-37.

Méheut, M., Lazzeri, M., Balan, E., Mauri, F., 2010. First-principles calculation of H/D isotopic fractionation between hydrous minerals and water. Geochim. Cosmochim. Acta. 74, 3874-3882.

Méheut, M., Schauble, E. A., 2014. Silicon isotope fractionation in silicate minerals: Insights from first-principles models of phyllosilicates, albite and pyrope. Geochim. Cosmochim. Acta. 134, 137-154.

Mei, Y., Sherman, D. M., Liu, W., Brugger, J., 2013. Ab initio molecular dynamics simulation and free energy exploration of copper(I) complexation by chloride and bisulfide in hydrothermal fluids. Geochim. Cosmochim. Acta. 102, 45-64.

Mei, Y., Sherman, D. M., Liu, W., Etschmann, B., Testemale, D., Brugger, J., 2015. Zinc complexation in chloride-rich hydrothermal fluids (25-600◦C): A thermodynamic model derived from ab initio molecular dynamics. Geochim. Cosmochim. Acta. 150, 265-284.

Mei, Y., Etschmann, B., Liu, W., Sherman, D. M., Testemale, D., Brugger, J., 2016. Speciation and thermodynamic properties of zinc in sulfur-rich hydrothermal fluids: Insights from ab initio molecular dynamics simulations and X-ray absorption spectroscopy. Geochim. Cosmochim. Acta. 179, 32-52.

Mei, Y., Liu, W., Migdisov, A. A., Brugger, J., Williams-Jones, A. E., 2018. CuCl Complexation in the Vapor Phase: Insights from Ab Initio Molecular Dynamics Simulations. Geofluids, doi.org 10.1155.2018.4279124.

Mei, Y., Liu, W., Brugger, J., Migdisov, A. A., Williams-Jones, A. E., 2017. Hydration is the key for gold transport in CO_2-HCl-H_2O vapour. ACS Earth Space Chem. 1(7), 368-375.

Mercadier, J., Richard, A., Cathelineau, M., 2012. Boron-and magnesium-rich marine brines at the origin of giant unconformity-related uranium deposits: δ^{11}B evidence from Mg-tourmalines. Geology 40, 231-234.

Meyer, C., Wunder, B., Meixner, A., Romer, R. L., Heinrich, W., 2008. Boron-isotope fractionation between tourmaline and fluid: an experimental re-investigation. Contrib. Mineral. Petrol. 156, 259-267.

Miller, Y., Chaban, G.M., Zhou, J., Asmis, K.R., Neumark, D.M., Gerber, R.B., 2007. Vibrational spectroscopy of $(SO_4^{2-})\cdot(H_2O)_n$ clusters, n=1-5: harmonic and anharmonic calculations and experiment. J. Chem. Phys. 127, 250.

Molnár, F., Mänttäri, I., O'Brien, H., Lahaye, Y., Pakkanen, L., Johanson, B., Käpyaho, A., Sorjonen-Ward, P., Whitehouse, M., Sakellaris, G., 2016. Boron, sulphur and copper isotope systematics in the orogenic gold deposits of the Archaean Hattu schist belt, eastern Finland. Ore Geol. Rev. 77, 133-162.

Morgan, G. B., London, D., 1989. Experimental reactions of amphibolite with boron-bearing aqueous fluids at 200 MPa: implications for tourmaline stability and partial melting in mafic rocks. Contrib. Mineral. Petrol. 102, 281-297.

Nakano, T., Nakamura, E., 2001. Boron isotope geochemistry of metasedimentary rocks and tourmalines in a subduction zone metamorphic suite. Phys. Earth & Planet. In. 127, 233-252.

Oi, T., Yanase, S., 2001. Calculations of Reduced Partition Function Ratios of Hydrated Monoborate Anion by the ab initio Molecular Orbital Theory. J. Nucl. Sci. Technol. 38, 429-432.

Palmer, M., London, D., Morgan, G., Babb, H., 1992. Experimental determination of fractionation of $^{11}B/^{10}B$ between tourmaline and aqueous vapor: A temperature-and pressure-dependent isotopic system. Chem. Geol. 101, 123-129.

Palmer, M. R., Slack, J. F., 1989. Boron isotopic composition of tourmaline from massive sulfide deposits and tourmalinites. Contrib. Mineral. Petrol. 103, 434-451.

Palmer, M. R., Swihart, G. H., 2002. Boron isotope geochemistry: an overview. Mineral. Soc. Am. 33, 709-744.

Peacock, S. M., Hervig, R. L., 1999. Boron isotopic composition of subduction-zone metamorphic rocks. Chem. Geol. 160, 281-290.

Pinilla, C., Blanchard, M., Balan, E., Natarajan, S. K., Vuilleumier, R., Mauri, F., 2015. Equilibrium magnesium isotope fractionation between aqueous Mg^{2+} and carbonate minerals: Insights from path integral molecular dynamics. Geochim. Cosmochim. Acta. 163, 126-139.

Pye, C. C., Rudolph, W. W., 2001. An ab Initio and Raman Investigation of Sulfate Ion Hydration. J. Phys. Chem. A. 105, 905-912.

Rajajee, V., Fletcher, J. J., Rochlen, L. R., Jacobs, T. L., 1999. Classification of the minerals of the tourmaline group. Euro. J. Mineral. 11, 201-216.

Rosner, M., Trumbull, R., Erzinger, J., Franz, G., 2003. Boron isotope fractionation during slab dehydration and across-arc $\delta^{11}B$ variations. *AGU Fall Meeting Abstracts*.

Rustad, J. R., Bylaska, E. J., 2007. Ab initio calculation of isotopic fractionation in $B(OH)_3$(aq) and $B(OH)_4^-$(aq). J. Am. Chem. Soc. 129, 2222-2223.

Rustad, J. R., Nelmes, S. L., Jackson, V. E., Dixon, D. A., 2008. Quantum-chemical calculations of carbon-isotope fractionation in CO_2(g), aqueous carbonate species, and carbonate minerals. J. Phys. Chem. A. 112, 542-555.

Rustad, J. R., Dixon, D. A., 2009. Prediction of Iron-Isotope Fractionation Between Hematite (α-Fe_2O_3) and Ferric and Ferrous Iron in Aqueous Solution from Density Functional Theory. J. Phys. Chem. A. 113, 12249.

Rustad, J. R., Yin, Q. Z., 2009. Iron isotope fractionation in the Earth's lower mantle. Nat. Geosci. 2, 514.

Rustad, J. R., Casey, W. H., Yin, Q. Z., Bylaska E. J., Felmy A. R., Bogatko S. A., Jackson V. E. and Dixon D. A., 2010a. Isotopic fractionation of Mg^{2+}(aq), Ca^{2+}(aq), and Fe^{2+}(aq) with carbonate minerals. Geochim. Cosmochim. Acta. 74, 6301-6323.

Rustad, J. R., Bylaska, E. J., Jackson, V. E., Dixon, D. A., 2010b. Calculation of boron-isotope fractionation between $B(OH)_3$(aq) and $B(OH)^{4-}$(aq). Geochim. Cosmochim. Acta. 74, 2843-2850.

Sanchez-Valle, C., Reynard, B., Daniel, I., Lecuyer, C., Martinez, I., Chervin, J. C., 2005. Boron isotopic fractionation between minerals and fluids: new insights from in situ high pressure-high temperature vibrational spectroscopic data. Geochim. Cosmochim. Acta. 69, 4301-4313.

Schauble, E.A., 2011. First-principles estimates of equilibrium magnesium isotope fractionation in silicate, oxide, carbonate and hexaaquamagnesium(2+) crystals. Geochim. Cosmochim. Acta. 75, 844-869.

Schreyer, W., Wodara, U., Marler, B., Seifert F., Robert, J. L., 2000. Synthetic tourmaline (olenite) with excess boron replacing silicon in the tetrahedral site. Eur. J. Mineral. 12, 529-541.

Schmidt, C., Thomas, R., Heinrich, W., 2005. Boron Speciation in Aqueous Fluids at 22 to 600°C and 0.1 MPa to 2 GPa. Geochim. Cosmochim. Acta. 69, 275-281.

Siegel, K., Wagner, T., Trumbull, R. B., Jonsson, E., Matalin, G., Wälle, M., Heinrich, C. A., 2016. Stable isotope (B, H, O) and mineral-chemistry constraints on the magmatic to hydrothermal evolution of the Varuträsk rare-element pegmatite (Northern Sweden). Chem. Geol. 421, 1-16.

Slack, J. F., 1996. Tourmaline associations with hydrothermal ore deposits. Revi. Mineral. Geochem. 33, 559-643.

Smith, M. P., Yardley, B. W. D., 1996. The boron isotopic composition of tourmaline as a guide to fluid processes in the southwestern England orefield: An ion microprobe study. Geochim. Cosmochim. Acta. 60, 1415-1427.

Su, Z. K., Zhao, X. F., Li, X. C., Zhou, M. F., 2016. Using elemental and boron isotopic compositions of tourmaline to trace fluid evolutions of IOCG systems: The worldclass Dahongshan FeCu deposit in SW China. Chem. Geol. 441, 265-279.

Tonarini, S., Dini, A., Pezzotta, F., Leeman, W. P., 1998. Boron isotopic composition of zoned (schorlelbaite) tourmalines, Mt. Capanne Li-Cs pegmatites, Elba (Italy). Eur. J. Mineral. 10, 941-952.

Vchirawongkwin, V., Rode, B.M., 2007. Solvation energy and vibrational spectrum of sulfate in water-An ab initio quantum mechanical simulation. Chem. Phys. Lett. 443, 152-157.

Wang, W., Qin, T., Zhou, C., Huang, S., Wu, Z., Huang, F., 2017. Concentration effect on equilibrium fractionation of Mg-Ca isotopes in carbonate minerals: Insights from first-principles calculations. Geochim. Cosmochim. Acta. 208, 185-197.

Widanagamage, I. H., Schauble, E. A., Scher, H. D., Griffith, E. M., 2014. Stable strontium isotope fractionation in synthetic barite. Geochim. Cosmochim. Acta. 147, 58-75.

Williams, L. B., Hervig, R. L., Holloway, J. R., Hutcheon, I., 2001. Boron isotope geochemistry during diagenesis. Part I. Experimental determination of fractionation during illitization of smectite. Geochim. Cosmochim. Acta. 65, 1769-1782.

Wu, Z. Q., Huang, F., Huang, S. C., 2015. Isotope fractionation induced by phase transformation: First-principle investigation for Mg_2SiO_4. Earth Planet. Sci. Lett. 409, 339-347.

Wunder, B., Meixner, A., Romer, R. L., Jahn, S., 2011. Li-isotope fractionation between silicates and fluids: Pressure dependence and influence of the bonding environment. Eur. J. Mineral. 23, 333-342.

Xavier, R. P., Wiedenbeck, M., Trumbull, R. B., Dreher, A. M., Monteiro, L. V., Rhede, D., de Araújo, C. E., Torresi, I., 2008. Tourmaline B-isotopes fingerprint marine evaporites as the source of high-salinity ore fluids in iron oxide copper-gold deposits, Carajas Mineral Province (Brazil). Geology. 36, 743-746.

Xue, C. J., Jiang, S. Y., Li, Y. H., 1997. Mineral Chemistry and boron isotopic composition of tourmaline from Shanyang-Zhuashui devonian metallogenic area in Eastern Qin Ling. Geochimica. 26(1), 36-44.

Yan, X. L., Chen B., 2014. Chemical and boron isotopic compositions of tourmaline from the Paleoproterozoic Houxianyu borate deposit, NE China: Implications for the origin of borate deposit. J. Asian Earth Sci. 94, 252-266.

Young, E. D., Manning, C. E., Schauble, E. A., Shahar, A., Macris, C. A., Lazar, C., Jordan, M., 2015. High-temperature equilibrium isotope fractionation of non-traditional stable isotopes: Experiments, theory, and applications. Chem. Geol. 395, 176-195.

Zeebe, R. E., 2005. Stable boron isotope fractionation between dissolved $B(OH)_3$ and $B(OH)_4^-$. Geochim. Cosmochim. Acta. 69, 2753-2766.

Zeebe, R. E., 2009. Hydration in solution is critical for stable oxygen isotope fractionation between carbonate ion and water. Geochim. Cosmochim. Acta. 73, 5283-5291.

Zeebe, R. E., 2010. A new value for the stable oxygen isotope fractionation between dissolved sulfate ion and water. Geochim. Cosmochim. Acta. 74, 818-828.

Zheng, Z., Deng, X. H., Chen, H. J., Yue, S. W., Dong, L. H., Qu, X., Chen, Y. J., 2016. Fluid sources and metallogenesis in the Baiganhu W–Sn deposit, East Kunlun, NW China: Insights from chemical and boron isotopic compositions of tourmaline. Ore Geol. Rev. 72, Part 1, 1129-1142.

Zhou, J., Santambrogio, G., Brümmer, M., Moore, D. T., Wöste, L., Meijer, G., Neumark, D. M., Asmis, K. R., 2006. Infrared spectroscopy of hydrated sulfate dianions. J. Chem. Phys. 125, 111102.

CAPTIONS OF FIGURES AND TABLES

Figure 1. Comparison on measured and computed vibrational frequencies for both isolated and aqueous H_3BO_3 and $B(OH)_4^-$ species at ambient condition. Experimental data were cited from

previous contributions (Kowalski et al., 2013 and references within). Theoretical values were calculated from clusters by B3LYP/6-31G(d).

Figure 2. Radial distribution functions of aqueous H_3BO_3 (abbreviated as B3) and $B(OH)_4^-$ (abbreviated as B4) from the AIMD simulations of the supercritical fluids (i.e. 0.5 GPa, 600K, 800K, 1000K). Insets are in-situ snapshots of hydrated boron species.

Figure 3. Histograms of the number of strong, moderate and weak hydrogen bonds of aqueous H_3BO_3 and $B(OH)_4^-$ in supercritical fluid. The statistics of hydrogen bonds were completed by the VMD program (Humphrey et al. 1996).

Figure 4. IR spectra of $H_3BO_3{\cdot}40H_2O$ at 0.5 GPa and 600 K, 800 K and 1000 K compared with the isolated and hydrated ones at ambient condition. Vibrational frequencies of $H_3BO_3{\cdot}40H_2O$ in supercritical fluid were calculated with individual configuration extracted from AIMD trajectories and only H_3BO_3 were relaxed with water molecules fixed in primitive high pressures/high temperature positions. At ambient condition, the frequencies of $H_3BO_3+32H_2O$ were calculated with fixing the surrounding water molecules. All calculations were completed with B3LYP/6-31G(d) combination.

Figure 5. Comparison of theoretically and experimentally determined boron isotope fractionation $1000\ln\alpha_{\text{Tur-fluid}}$ versus reciprocal temperature between dravite and fluids under various conditions. The shadow area is the calculated error of Kowalski et al. (2013). The black diamonds and solid line represent our prediction for the boron isotope fractionation between dravite and acidic fluid containing only B^{III}. The black dash lines are our prediction for the boron isotope fractionation between dravite and neutral fluid containing 10% and 15% B^{IV}. The error bars in all data correspond to 2σ, and all data are fitted with the linear regression.

Figure 6. Comparison of equilibrium boron isotope fractionation of tourmaline with different composition. All models optimized with B3LYP/6-31G(d). The overall errors in $\Delta^{11}B_{(\text{tour-fluid})}$ were estimated to be ± 1.9‰, ± 1.7‰ and ± 1.0‰ at 600 K, 800 K and 1000 K, at the same level with Kowalski et al. (2013). The chemical compositions of tourmaline group represented by models were listed as follow: Dravite: $NaMg_3Al_6[Si_6O_{18}][BO_3]_3(OH)_4$; Mg-foitite: $Mg_2AlAl_6[Si_6O_{18}][BO_3]_3(OH)_4$; Dravite+Fe: $Na(Mg_2Fe)Al_6[Si_6O_{18}][BO_3]_3(OH)_4$; Olenite:

$NaAl_3Al_6[Si_6O_{18}][BO_3]_3O_3(OH)$; Fluor-dravite: $NaMg_3Al_6[Si_6O_{18}][BO_3]_3(OH)_3F$; Schorl: $NaFe_3Al_6[Si_6O_{18}][BO_3]_3(OH)_4$; Schorl+Mg: $Na(Fe_2Mg)Al_6[Si_6O_{18}][BO_3]_3(OH)_4$; Hydroxy-liddicoatite: $CaMgLi_2Al_6[Si_6O_{18}][BO_3]_3(OH)_4$.

Figure 7. (a) Dependence of $1000\ln\alpha_{\text{Tur-fluid}}$ on the average B-O bond lengths in tourmaline group minerals at 1000 K, 800 K and 600 K; (b) Dependence of the B-O bond length on the Mg content in the solid solution.

Figure 8. Relationship of boron isotope fractionation between tourmalines and fluids with *S* at 1000 K, 800 K and 600 K (a), and with the *M/E* ratios at 600 K (b). *S* is the sum of products of metal ion radius and apparent charge in *X* and *Y* sites of the tourmaline. M and E, respectively, are the atomic weights and the apparent charge of metal atoms in *X* and *Y* sites of the tourmaline models. The metal ion radii and atomic weights of metals at sites of *X*, *Y*, *Z* are from Ignatiev (2005) and Coplen (2001).

Figure 9. Crystallization sequence of seven tourmalines according to the Gibbs free energy of formation calculated with B3LYP/6-31G(d). From core to rim, the individual colors present schorl, schorl+Mg, dravite+Fe, hydroxy-liddicoatite, olenite, dravite (or fluor-dravite) and Mg-foitite respectively.

Table 1. Dependence of $1000\ln\alpha_{\text{tour-fluid}}$ on the average B-O bond length in different tourmalines

Table 2. Dependence of $1000\ln\alpha_{\text{Tur-fluid}}$ on the sum of products of metal ion radius and apparent charge in *X*, *Y* and *Z* sites of tourmaline